UCSD/PTH/97-05
UK/97-02
hep-lat/9704011

Efficient glueball simulations on anisotropic lattices

Colin J. Morningstar
Dept. of Physics, University of California at San Diego, La Jolla, California 92093-0319

Mike Peardon
Department of Physics and Astronomy, University of Kentucky, Lexington, KY 40506-0055

(April 22, 1997)

Abstract

Monte Carlo results for the low-lying glueball spectrum using an improved, anisotropic action are presented. Ten simulations at lattice spacings ranging from 0.2 to 0.4 fm and two different anisotropies have been performed in order demonstrate the advantages of using coarse, anisotropic lattices to calculate glueball masses. Our determinations of the tensor (2^{++}) and pseudovector (1^{+-}) glueball masses are more accurate than previous Wilson action calculations.

PACS number(s): 11.15.Ha, 12.38.Gc, 12.39.Mk

I. INTRODUCTION

Numerical simulations of gluons on a space-time lattice provide at present the most reliable means of studying glueballs. Glueball correlation functions are, however, notoriously difficult quantities to measure in Monte Carlo simulations: since the masses of these states are rather high and their creation operators have large vacuum fluctuations, the signal-to-noise ratio falls extremely rapidly as the separation between the source and sink is increased. Because of this, reliable studies of glueballs on fine lattices have required prohibitively large computer resources. Thus, the development of more efficient simulation techniques in lattice QCD is crucial to establishing a detailed description of glueballs and their interactions.

The objective of this work is to examine the effectiveness of using an improved, anisotropic lattice action to reduce the computational effort needed to determine the glueball spectrum in quenched QCD. Improved actions allow access to continuum physics on coarser lattices than possible using the simple Wilson discretization. Coarse lattice simulations are more efficient for several reasons: for a given physical volume, much fewer lattice sites are needed; the alleviation of critical slowing down permits the faster generation of statistically independent gauge-field configurations; glueball operator smearing is faster due to the decreased number of links and a decrease in the number of smearing iterations required; glueball wavefunctions extend over much fewer lattice sites on a coarse lattice, making the variational technique far more effective when using a feasible number (a dozen or so) of basis operators.

However, for glueball mass calculations, the coarseness of the temporal lattice spacing is a severe drawback. As the masses in lattice units of the states of interest are so large, the number of correlator time intervals which can be measured is reduced greatly [1]. A straightforward solution to this problem which preserves the computational advantages of coarse lattices[2, 3, 4] is to make use of anisotropic lattices in which the temporal spacing is much smaller than that in the spatial directions. This enables us to exploit the enhanced signal-to-noise of the correlation functions at smaller temporal separations. A natural scale for the temporal lattice spacing should be the inverse of the energy of the states of interest; thus, for glueballs, a temporal cut-off larger than 1.5 GeV allows resolution from accessible statistics of the correlator over a few time-slices. Meanwhile, the scale for the spatial lattice should be set by the size of the wavefunction of the state; a spatial grid separation in the range $0.2 - 0.4$ fm would seem reasonable.

Since we propose to use lattices in which the temporal lattice spacing is small, improvement of the discretization in this direction is not needed. Thus, a lattice action which couples only nearest-neighbor time-slices can be used. The transfer matrix corresponding to such an action is Hermitian and positive definite; all of our effective masses must converge to their plateau values monotonically from above. This ensures the validity of variational techniques which minimize the effective masses at small temporal separations. Such techniques are very effective in diminishing the excited-state contributions to the glueball correlation functions and are crucial for efficient extraction of ground-state masses.

In this paper, we demonstrate the increased efficiency of glueball simulations using these actions on anisotropic lattices. We present results for the masses of three of the lighter SU(3) glueball states, the scalar (0^{++}), the tensor (2^{++}), and the pseudovector (1^{+-}). The masses of the first excited states in the scalar and tensor channels were also examined.

Ten simulations at lattice spacings ranging from 0.2 to 0.4 fm were performed, enabling reliable extrapolations to the continuum limit (although the mass of the scalar glueball was somewhat problematic). The results are compared to previous simulation data obtained using the Wilson action and we find that more accurate determinations of the tensor and pseudovector glueball masses have been achieved. A comparison of efficiencies is also made. Lastly, finite volume effects are shown to be small.

The new action used in our simulations is described in Sec. II. The details of the glueball simulations, including the construction of the glueball operators, the generation of the gauge-field configurations, and the analysis of the Monte Carlo data, are given in Sec. III. The hadronic scale r_0 is used to relate our results at different values of the coupling β and the aspect ratio ξ. The determination of this scale in terms of the lattice spacing using the static potential is outlined in Sec. IV. Sec. V contains our results and discussion: the glueball mass measurements are presented in detail; finite volume effects are studied; extrapolations of the masses at finite spacing to the continuum limit are undertaken; the conversion of our results into physical units is described; and a comparison of efficiencies with Wilson action simulations is made. Our conclusions are given in Sec. VI, along with an outline of future work.

II. AN IMPROVED, ANISOTROPIC DISCRETIZATION OF QCD

Our glueball mass determinations rely on numerical simulations of glueballs on a Euclidean space-time lattice with spatial and temporal spacings a_s and a_t, respectively. The improved gluonic action used in this study is given by [2, 4]

$$S_{II} = \beta \left\{ \frac{5}{3}\frac{\Omega_{\rm sp}}{\xi u_s^4} + \frac{4}{3}\frac{\xi\Omega_{\rm tp}}{u_s^2 u_t^2} - \frac{1}{12}\frac{\Omega_{\rm sr}}{\xi u_s^6} - \frac{1}{12}\frac{\xi\Omega_{\rm str}}{u_s^4 u_t^2} \right\}, \tag{1}$$

where $\beta = 6/g^2$, g is the QCD coupling, u_s and u_t are mean link renormalization parameters, ξ is the aspect ratio ($\xi = a_s/a_t$ at tree level in perturbation theory), and $\Omega_C = \sum_C \frac{1}{3}{\rm Re\ Tr}(1 - W_C)$, with W_C denoting the path-ordered product of link variables along a closed contour C on the lattice. $\Omega_{\rm sp}$ includes the sum over all spatial plaquettes on the lattice, $\Omega_{\rm tp}$ indicates the temporal plaquettes, $\Omega_{\rm sr}$ denotes the product of link variables about planar 2×1 spatial rectangular loops, and $\Omega_{\rm str}$ refers to the short temporal rectangles (one temporal link, two spatial). Explicitly,

$$\Omega_{\rm sp} = \sum_x \sum_{i>j} \tfrac{1}{3}{\rm ReTr}\left[1 - U_i(x)U_j(x+\hat\imath)U_i^\dagger(x+\hat\jmath)U_j^\dagger(x)\right], \tag{2}$$

$$\Omega_{\rm tp} = \sum_x \sum_{i} \tfrac{1}{3}{\rm ReTr}\left[1 - U_t(x)U_i(x+\hat t)U_t^\dagger(x+\hat\imath)U_i^\dagger(x)\right], \tag{3}$$

$$\Omega_{\rm sr} = \sum_x \sum_{i\neq j} \tfrac{1}{3}{\rm ReTr}\left[1 - U_i(x)U_i(x+\hat\imath)U_j(x+2\hat\imath)U_i^\dagger(x+\hat\imath+\hat\jmath)U_i^\dagger(x+\hat\jmath)U_j^\dagger(x)\right], \tag{4}$$

$$\Omega_{\rm str} = \sum_x \sum_{i} \tfrac{1}{3}{\rm ReTr}\left[1 - U_i(x)U_i(x+\hat\imath)U_t(x+2\hat\imath)U_i^\dagger(x+\hat\imath+\hat t)U_i^\dagger(x+\hat t)U_t^\dagger(x)\right], \tag{5}$$

where x labels the sites of the lattice, i, j are spatial indices, and $U_\mu(x)$ is the parallel transport matrix in the gluon field from site x to $x+\hat\mu$.

This action, intended for use with $a_t \ll a_s$, has $O(a_s^4, a_t^2, \alpha_s a_s^2)$ discretization errors. The $O(a_t^2)$ errors can be removed by the addition of counterterms which couple next-nearest-neighbor time-slices, but this introduces spurious high-energy modes which can cause considerable problems for our glueball simulations. These unphysical states appear in perturbation theory as additional poles in the gluon propagator. Their detrimental effects on the glueball correlation functions have been previously demonstrated[1]. Although these spurious states do not affect the asymptotic behavior of the glueball correlators, they do appreciably change the correlators at short temporal separations and can seriously hinder attempts to reduce excited-state contamination to hasten the onset of asymptotic behavior. Since our glueball mass measurements rely heavily on the reduction of such excited-state contributions to the glueball correlation functions, the use of an action which is free of spurious lattice modes is crucial. The action given in Eq. 1 couples only link variables on neighboring time-slices, which ensures that all of our effective masses converge to their plateau values monotonically from above and so validates the variational techniques employed.

It is now known that perturbation theory by itself does not reliably determine the couplings in an improved action in lattice gauge theory. Hence, the interaction strengths in S_{II} have been determined using a judicious combination of perturbation theory and mean field theory. Mean field theory is introduced by separately renormalizing the spatial and temporal link variables: $U_j(x) \to U_j(x)/u_s$ and $U_t(x) \to U_t(x)/u_t$, where u_s and u_t denote the renormalization factors for the spatial and temporal links, respectively. The mean-link parameters u_t and u_s are best determined by guessing input values for use in the action, measuring the mean links in Landau gauge in a simulation, then readjusting the input values accordingly and tuning until the input values match the measured values. The determination of these renormalization factors is described in more detail in Refs. [2, 4]. However, when a_t is significantly smaller than a_s, we expect the mean temporal link u_t to be very close to unity since $1 - \langle \frac{1}{3}\mathrm{Tr}U_t \rangle \propto (a_t/a_s)^2$ in perturbation theory. Hence, to simplify matters, we set $u_t = 1$. We introduce further simplifications by using a convenient and gauge-invariant definition for u_s in terms of the mean spatial plaquette given by $u_s = \langle \frac{1}{3}\mathrm{ReTr}P_{ss'} \rangle^{1/4}$, where $P_{ss'}$ denotes the spatial plaquette. This eliminates the need for gauge fixing, yields values for u_s which differ from those found using the Landau gauge definition by only a few per cent, and significantly speeds up the tuning process.

At finite coupling g, the anisotropy a_s/a_t is renormalized away from its input value ξ. Measurements of this renormalization have been made using the static potential extracted from correlations along the different spatial and temporal axes of the lattice [2, 4]. Without mean-link improvement, this renormalization can be as large as 30%. When the action includes mean-link corrections, this renormalization is found to be small, typically a few per cent. We used $a_t/a_s = \xi$ in all of our calculations, accepting the small radiative corrections to the anisotropy as finite lattice spacing errors, which vanish in the continuum limit.

III. GLUEBALL SIMULATION DETAILS

Glueballs may be labeled by their total (integral) spin J and their symmetries under spatial inversion and charge conjugation. However, on a cubic lattice, glueballs are characterized by their transformation properties under the cubic point group, combined with parity and charge conjugation operations. The cubic group, O_h, has 24 elements that fall into five conjugacy classes, and thus, the dimensions of the irreducible representations (irreps) are 1, 1, 2, 3 and 3. These irreps are labeled A_1, A_2, E, T_1, and T_2, respectively. Including parity and charge conjugation symmetry operations, there are 20 irreps (labeled by J^{PC}, where J now denotes an irrep of O_h). In this study, four of the irreps which generate light (< 3 GeV) glueball states were simulated: the A_1^{++}, E^{++}, T_2^{++}, and T_1^{+-} channels. Of particular interest are the E^{++} and T_2^{++} irreps whose combined five rows correspond to the five polarization states of the tensor (2^{++}) glueball which become degenerate as continuum rotational invariance is restored. This then gives information on the magnitude of lattice artifacts at finite cut-off.

The mass of a glueball, G, having a given J^{PC} can be extracted from the large-t behavior of a correlation function $C(t) = \langle 0|\bar{\Phi}^{(R)\dagger}(t)\ \bar{\Phi}^{(R)}(0)|0\rangle$, where R denotes the lattice irrep corresponding to the J^{PC} of interest and $\bar{\Phi}^{(R)}(t) = \Phi^{(R)}(t) - \langle 0|\Phi^{(R)}(t)|0\rangle$ is a gauge-invariant, translationally-invariant, vacuum-subtracted operator capable of creating a glueball out of the QCD vacuum $|0\rangle$. As the temporal separation t becomes large, this correlator tends to a single decaying exponential $\lim_{t\to\infty} C(t) = Z\exp(-m_G t)$, where m_G is the mass of the lowest-lying glueball which can be created by the operator $\bar{\Phi}^{(R)}(t)$. In order to extract m_G, the correlator $C(t)$ must be determined for t sufficiently large that $C(t)$ is well approximated by its asymptotic form. However, the signal-to-noise ratio in any Monte Carlo determination of $C(t)$ falls exponentially fast with respect to t. Thus, it is crucial to use a glueball operator for which $C(t)$ attains its asymptotic form as quickly as possible. If $|G\rangle$ denotes the glueball state of interest, this means that we must choose an operator for which the overlap $\langle G|\bar{\Phi}^{(R)}(t)|0\rangle / [\langle G|G\rangle\langle 0|\bar{\Phi}^{(R)\dagger}(t)\bar{\Phi}^{(R)}(t)|0\rangle]^{1/2}$ is as near to unity as possible. For such an operator, the signal-to-noise ratio is also optimal[5].

In order to construct such operators, we exploited the smearing [6, 7] and variational techniques which have been used with success in earlier Wilson action simulations. In each of the J^{PC} channels of interest, glueball operators were constructed on each time-slice in a sequence of three steps. First, smeared links $U_j^s(x)$ and fuzzy superlinks $U_j^f(x)$ were formed. Secondly, a set of basic operators $\phi_\alpha^{(R)}(t)$ were constructed using linear combinations of gauge-invariant, path-ordered products of the $U_j^s(x)$ and $U_j^f(x)$ matrices about various closed spatial loops; each such linear combination was designed to be invariant under spatial translations and to transform irreducibly under the symmetry operations of the cubic point group according to the irrep of interest. Lastly, the glueball operators $\Phi^{(R)}(t)$ were formed from linear combinations of the basic operators, $\Phi^{(R)}(t) = \sum_\alpha v_\alpha^{(R)}\phi_\alpha^{(R)}(t)$, where the coefficients $v_\alpha^{(R)}$ were determined using the variational method. Each of these three steps is described below.

Operators constructed out of smeared links and fuzzy superlinks have dramatically reduced mixings with the high frequency modes of the theory. Thus, the use of spatially-smoothed links is an important part of reducing excited-state contamination in the glueball correlation functions. Two smoothing procedures were used: a single-link procedure and a double-link procedure. In the single-link procedure, every spatial link $U_j(x)$ on the lattice is replaced by itself plus a sum of its four neighboring (spatial) staples, projected back into SU(3):

$$U_j^s(x) = \mathcal{P}_{SU(3)} \left\{ U_j(x) + \lambda_s \sum_{\pm(k\neq j)} U_k(x)\, U_j(x+\hat{k})\, U_k^\dagger(x+\hat{j}) \right\}, \tag{6}$$

where $\mathcal{P}_{SU(3)}$ denotes the projection [8] into SU(3). Here, we denote this mapping of the spatial link matrices into the smeared link variables by s_{λ_s}. In the double-link procedure, new superlinks U^f of length $2a_s$ are built using neighboring staples which connect sites separated by a distance twice that of the length of the source link variables:

$$\begin{aligned} U_j^f(x) = \mathcal{P}_{SU(3)} \Big\{ & U_j(x)\, U_j(x+\hat{j}) \\ & + \lambda_f \sum_{\pm(k\neq j)} U_k(x)\, U_j(x+\hat{k})\, U_j(x+\hat{j}+\hat{k})\, U_k^\dagger(x+2\hat{j}) \Big\}, \end{aligned} \tag{7}$$

and we denote this mapping by f_{λ_f}. Both procedures can be applied recursively; smeared links can be smeared again and fuzzy links of increasing length $2a_s$, $4a_s$, $8a_s \ldots$ can be constructed. A *smoothing scheme*, $\mathcal{S}$, is defined as a composition of single-link mappings and double-link mappings. Six different smoothing schemes were used. The simplest scheme used was the composition of two single-link smearings: $\mathcal{S}_1 = s_{\lambda_s} \circ s_{\lambda_s}$. To simplify notation, we write this as $\mathcal{S}_1 = s^2_{\lambda_s}$. We also used the compositions of four and six single-link mappings: $\mathcal{S}_2 = s^4_{\lambda_s}$ and $\mathcal{S}_3 = s^6_{\lambda_s}$. In the other three smoothing schemes, the application of several single-link smearings, followed by one final iteration of double-link fuzzing was used: $\mathcal{S}_4 = f_{\lambda_f} \circ s^2_{\lambda_s}$, $\mathcal{S}_5 = f_{\lambda_f} \circ s^4_{\lambda_s}$, and $\mathcal{S}_6 = f_{\lambda_f} \circ s^6_{\lambda_s}$. Only one iteration of the fuzzing procedure which results in links connecting sites separated by $2a_s$ was found to be useful for the range of coarse a_s values explored here. For the finer lattices ($\beta = 2.4, \xi = 5$ and $\beta = 2.6, \xi = 3$), an extra four initial iterations of single-link smearing were used in all six smoothing schemes to enhance ground-state overlap. To simplify matters, the same values for the two parameters λ_s and λ_f were used in all smearing and fuzzing iterations. These values were chosen to minimize excited-state contamination in the glueball correlation functions. A crude optimization was done in a set of low statistics runs and the optimal values $\lambda_s = 0.1$ and $\lambda_f = 0.5$ were then used in all the glueball simulations.

The second step in the construction of our glueball operators was the formation of a set of basic operators $\phi_\alpha^{(R)}(t)$ using linear combinations of gauge-invariant, path-ordered products of the $U_j^s(x)$ and $U_j^f(x)$ matrices about various closed spatial loops. Combinations which were Hermitian, invariant under spatial translations, and transformed irreducibly under the operations of the cubic point group according to the irrep of interest were constructed. For a more detailed exposition of this construction, see Ref. [9]. In each channel, a large set of prototypes were programmed, and a short simulation was then performed to determine the coefficients of each operator in the variational ground state. In each channel, the four operators with the highest of these contributions were then chosen for use in the production runs. The paths in this optimal set are illustrated in Fig. 1. In the glueball simulations, these Wilson loops were measured on the link variables from the six smoothing schemes, yielding a total of $N = 24$ basic operators $\phi_\alpha^{(R)}(t)$ in each of the four channels.

Finally, $\Phi^{(R)}(t)$ was formed from a linear combination of the basic operators, $\Phi^{(R)}(t) = \sum_{\alpha=1}^N v_\alpha^{(R)} \phi_\alpha^{(R)}(t)$. The coefficients $v_\alpha^{(R)}$ were determined using the variational method. First, the 24×24 correlation matrix was computed in the glueball simulations:

$$\tilde{C}_{\alpha\beta}(t) = \sum_{\tau} \langle 0|\bar{\phi}^{(R)}_{\alpha}(\tau+t)\, \bar{\phi}^{(R)}_{\beta}(\tau)|0\rangle, \tag{8}$$

where $\bar{\phi}^{(R)}_{\alpha}(t)$ denotes a vacuum-subtracted operator $\bar{\phi}^{(R)}_{\alpha}(t) = \phi^{(R)}_{\alpha}(t) - \langle 0|\phi^{(R)}_{\alpha}(t)|0\rangle$. Note that $\langle 0|\phi^{(R)}_{\alpha}(t)|0\rangle$ is independent of t. The coefficients $v^{(R)}_{\alpha}$ were then determined by minimizing the effective mass

$$\tilde{m}(t_D) = -\ln\left[\frac{\sum_{\alpha\beta} v^{(R)}_{\alpha} v^{(R)}_{\beta}\ \tilde{C}_{\alpha\beta}(t_D)}{\sum_{\alpha\beta} v^{(R)}_{\alpha} v^{(R)}_{\beta}\ \tilde{C}_{\alpha\beta}(0)}\right], \tag{9}$$

where the time separation for optimization was fixed in all cases to $t_D = 1$. Let $\mathbf{v}^{(R)}$ denote a column vector whose elements are the optimal values of the coefficients $v^{(R)}_{\alpha}$. Then requiring $d\tilde{m}(t_D)/dv^{(R)}_{\alpha} = 0$ for all α yields an eigenvalue equation:

$$\tilde{C}(t_D)\ \mathbf{v}^{(R)} = e^{-\tilde{m}(t_D)}\ \tilde{C}(0)\ \mathbf{v}^{(R)}. \tag{10}$$

The eigenvector $\mathbf{v}^{(R)}_0$ corresponding to the largest eigenvalue $e^{-\tilde{m}_0(t_D)}$ then yields the coefficients $v^{(R)}_{0\alpha}$ for the operator $\Phi^{(R)}_0(t)$ which best overlaps the lowest-lying glueball G in the channel of interest. Operators which overlap excited glueball states can also be constructed using the other eigenvectors of Eq. 10. In particular, the operator $\Phi^{(R)}_1(t)$ expected to best overlap the first-excited glueball state G^* was obtained from the eigenvector corresponding to the second largest eigenvalue of Eq. 10.

The elements of the correlator matrix given in Eq. 8 were estimated using the Monte Carlo method. Ten separate glueball simulations were performed on DEC Alpha-workstations. Configuration ensembles were generated using both Cabibbo-Marinari (CM) pseudo-heatbath and $SU(2)$ sub-group over-relaxation (OR) methods. Link variables were updated in serial order on the lattice. We define a *compound sweep* as one CM updating sweep followed by three OR sweeps. In the glueball simulations, three compound sweeps were performed between measurements, and the measurements were averaged into bins of 100 in order to reduce data storage requirements (except for the $\beta = 2.6$, $\xi = 3$ run in which 40 configurations were included in each bin). In all ten simulations, 100 bins were obtained. Our ensembles were tested for residual autocorrelations during the analysis phase by over-binning by factors of two and four; in all cases, the statistical error estimates remained unchanged.

Values for the mean link parameter u_s were determined self-consistently as previously described. This tuning procedure required a minimal amount of computational effort and provided thermalized configurations for later computations. The improved action simulation parameters used are given in Table I.

For the data-fitting phase, the large 24×24 correlator matrices in each channel were reduced using the coefficients $\mathbf{v}^{(R)}_0$ and $\mathbf{v}^{(R)}_1$ to smaller 2×2 matrices $C_{AB}(t)$ for $A, B = 0, 1$:

$$C_{AB}(t) = \sum_{\tau} \langle 0|\bar{\Phi}^{(R)}_{A}(\tau+t)\ \bar{\Phi}^{(R)}_{B}(\tau)|0\rangle. \tag{11}$$

The ground-state correlator $C_{00}(t)$ was fit for $t = t_{\min}, \ldots, t_{\max}$ using a single exponential

$$C_{00}(t) = Z_{00}\left\{e^{-m_G t} + e^{-m_G(T-t)}\right\}, \tag{12}$$

where T was the temporal extent of the periodic lattice, to obtain an estimate of the mass m_G (in terms of a_t^{-1}) of the lowest-lying glueball in each channel. To determine the mass m_{G^*} of the first-excited glueball and another estimate of m_G, the 2×2 correlator was also fit for $t = t_{\rm min}, \ldots, t_{\rm max}$ using the form

$$C_{AB}(t) = \sum_{p=G,G^*} Z_{Ap} Z_{Bp} \left\{ e^{-m_p t} + e^{-m_p(T-t)} \right\}. \qquad (13)$$

Various fit regions $t_{\rm min}$ to $t_{\rm max}$ were used in order to check for consistency in the extracted values for the masses. Best fit values were obtained using the correlated χ^2 method. Error estimates were calculated using a 1024−point bootstrap procedure; in all cases, error estimates were very close to being symmetric about the central best-fit values and were thus averaged to simplify presentation.

IV. SETTING THE SCALE USING THE STATIC POTENTIAL

In order to convert the glueball masses as measured in our simulations into physical units, we must set the scale by determining the lattice spacing a_t for each β and ξ we consider. To do this, we must first choose one physical quantity to use as a reference. This reference quantity must then be measured on the lattice in terms of a_t. The experimentally-known value for the reference quantity is then used to extract the lattice spacing. A quantity which can be easily and accurately determined both experimentally and in numerical simulations is an ideal choice for such a reference. The mass of a low-lying particle is typically used for setting the scale. In our case, however, there are no unambiguous experimental determinations of the glueball masses, so instead, we must look for another purely gluonic quantity.

The hadronic scale parameter r_0 defined in terms of the force between static quarks by $[r^2 dV(\vec{r})/dr]_{r=r_0} = 1.65$, where $V(\vec{r})$ is the static-quark potential, is an attractive possibility. It can be measured very accurately on the lattice. The advantages in using r_0 to set the scale have been enumerated in Ref. [10]. From phenomenological potential models, one finds $r_0 \approx 0.5$ fm. A disadvantage in using r_0 is that its physical value must be deduced indirectly from experiment, and there is some ambiguity in doing this, as will be discussed below. However, in the absence of a better gluonic reference, we have chosen r_0 to set the scale. In this section, we outline the determination of r_0 in terms of a_s.

In order to determine r_0 in terms of the lattice spacing, we need accurate measurements of the static-quark potential. We extracted $V(\vec{r})$ for various spatial separations $\vec{r}$, both on and off the axes of the lattice, from the expectation values of Wilson loops $W(\vec{r}, t)$ in the standard manner:

$$W(\vec{r}, t) = Z(\vec{r}) \ \exp[-tV(\vec{r})] + \text{excited state contributions}. \qquad (14)$$

In the Monte Carlo evaluation of the Wilson loops, measurements were taken after every four compound sweeps (as defined in Sec. III). The measurements of the Wilson loops were done independently of the glueball mass studies using separate ensembles of configurations. To minimize contamination from excited states, the Wilson loops were constructed from iteratively smeared spatial links. The single-link smearing method described previously was used. A given smearing scheme is specified not only by the parameter λ_s, but also by the total number of smearing iterations, denoted by n_λ. Two different choices of the smearing parameter were used in all cases: one smearing was chosen to work well for small $r = |\vec{r}|$, the other to work well for large r. Separate measurements for each smearing were taken; cross correlations were not determined. The statistical noise in the evaluation of $W(\vec{r}, t)$ was reduced dramatically, especially for large temporal separations, by constructing the Wilson loops, whenever possible, from thermally-averaged temporal links [11]. The thermal averaging was accomplished using the Cabibbo-Marinari pseudo-heatbath method (40 updates). Other relevant run parameters are given in Table II.

The values of the potential $V(\vec{r})$ were extracted from the Wilson loop measurements by fitting $W(\vec{r}, t)$ to the exponential form $Z(\vec{r})\exp[-tV(\vec{r})]$ in the range $t = t_{\rm min}, \ldots, t_{\rm max}$, for each $\vec{r}$. The plateau region from $t_{\rm min}$ to $t_{\rm max}$ was chosen separately for each $\vec{r}$ in order to minimize the uncertainty in the extracted values for $V(\vec{r})$ while maintaining a good quality Q of fit. Best fit values were determined using the standard χ-square test, taking into account temporal correlations among the $W(\vec{r}, t)$. The covariance matrix in χ^2 was determined using the jack-knife procedure, and estimates for the uncertainties in the extracted values for $V(\vec{r})$ were computed using the bootstrap method. Binning of the data was done as a crude check that our measurements were statistically independent. The results of a typical fit are shown in Fig. 2, which is an effective mass plot for $V(\vec{r})$ for $\vec{r}/a_s = (2, 2, 2)$. The effective mass for $V(\vec{r})$ is a function of t, defined as $\ln[W(\vec{r}, t)/W(\vec{r}, t + a_t)]$, which tends to the true mass as t becomes large.

Once a suitable plateau region in the effective mass was established for each $V(\vec{r})$, the hadronic scale r_0/a_s could be determined. We found that the on-axis potential $V(\vec{r})$ for the range of $\vec{r}$ values studied here using coarse lattices fit a Coulomb plus linear form $V(\vec{r}) = e_c/r + \sigma r + V_0$ very well (with qualities of fit ranging from $Q = 0.25$ to $Q = 0.99$). We, therefore, used this form to interpolate $V(\vec{r})$ and the force between static quarks. Simultaneous fits of the Wilson loops for the on-axis potential to the form $Z(r)\ \exp[-t(e_c/r + \sigma r + V_0)]$ were done, taking into account all correlations among the $W(r, t)$ for both different t and r. Different regions in t were used for different r values; the plateau regions determined previously were used. Only the on-axis potentials were used; this prevented the covariance matrix in the χ^2 to be minimized from getting too large. This covariance matrix was evaluated using the jack-knife method; uncertainties in the fit parameters e_c, σ, V_0, and $Z(r)$ were obtained using the bootstrap method. Once we had an ensemble of bootstrap estimates for these fit parameters, the ratio r_0/a_s and its bootstrap uncertainty were then determined using

$$r_0/a_s = \sqrt{(1.65 + e_c)/\sigma a_s^2}. \tag{15}$$

Note that to compute r_0/a_s, we need the ratio a_s/a_t since our fits yielded estimates of $a_t V(\vec{r})$ only. We used the input value ξ since we know that its renormalization is small. Results for r_0/a_s are given in Table III.

Using the results in Table III, we can now express all energies measured in simulations in terms of r_0. For example, in Fig. 3, we show the potential, including off-axis inter-quark separations, expressed in terms of r_0. Lattice spacing errors are seen to be small.

V. RESULTS AND DISCUSSION

A. Glueball mass measurements

To allow clear resolution of the scaling properties of the low-lying glueball masses in the improved action, two sets of simulations were performed at two different anisotropies: six lattice spacings for an aspect ratio $\xi = 3$ and four spacings for $\xi = 5$ were studied. The input parameters used in these simulations are given in Table I.

The results of fitting the variationally-optimized correlators $C(t)$ to the functions given in Eqs. 12 and 13 are summarized in Tables IV-XIII. Effective mass plots for the two smallest-a_s simulations are presented in Figs. 4−7 and Figs. 8−11 for $\xi = 3$ and $\xi = 5$, respectively. For each channel in each of the ten simulations, it was possible to find a fit region $t_{\min} - t_{\max}$ in which the correlation function was well described by its asymptotic form as indicated by the quality of fit. In other words, convincing plateaux were observed in all effective masses. The most impressive plateau, observed in the A_1^{++} channel for $\beta = 2.4$ and $\xi = 5$, spanned ten time-slices. In most cases, the onset of the plateau occurred when the source and sink operators were separated by only one time-step. The overlaps with the lowest-lying states were also found to be extremely good, better than 90% in most cases and often consistent with unity. This clearly demonstrates the effectiveness of the link-smearing and variational techniques in diminishing excited-state contamination. Fits using $t_{\min} = 2$ or 0 were also done to check for agreement with the $t_{\min} = 1$ results. At time separations for which the ground state could be reliably observed, the off-diagonal elements of the reduced correlation matrices $C_{AB}(t)$ were found to be consistent with zero within statistical uncertainty. This suggests that the link-smearing, variational method also gives an excellent construction of the first-excited state in each channel.

Our best estimates for the glueball masses in terms of a_t^{-1} are indicated in boldface in each of the Tables IV-XIII. These estimates are summarized in Table XIV. Masses for the first-excited states are also indicated in the $N_{exp} = 2$ fits listed in the Tables IV-XIII.

B. Finite volume effects

In this work, we were concerned with the magnitude of discretization errors in the glueball mass determinations from coarse lattice simulations using an improved action. In order to evaluate these errors, we had to eliminate uncertainties from all other sources. The increased efficiency of simulations on coarse, anisotropic lattices allowed us to reduce statistical errors to the acceptable level of about 1%. The only remaining source of uncertainty we had to address was finite volume. The masses of particles confined in a small box with periodic boundary conditions can differ appreciably from their infinite volume values; finite volume effects can also induce a splitting in the masses of the E and T_2 tensor polarizations. Finite volume effects on the scalar glueball mass have been analyzed before[12], but the effects on the tensor and the pseudovector are less well known.

In order to ascertain the effects on our glueball masses of simulating in a finite volume, four extra simulations were performed for $\beta = 2.4$, $\xi = 3$ using lattices of spatial extent $L_s/a_s = 6, 5, 4$, and 3. The temporal extent was held fixed at 24 grid points. For each of these volumes, the mean-field renormalization parameter u_s was recalculated. The 3^3 lattice was the only simulation that required any change in this parameter, and in this case, the effect was small; u_s increased by only 0.3%. The results from the $L_s/a_s = 8, 6, 5$, and 4 runs for the glueball masses in terms of a_t^{-1} are given in Table XV. Note that the results from the 6^3 lattice differ very little from those from the 8^3 lattice, suggesting that our lattice volumes are sufficiently large to ensure that finite volume errors are negligible. For the 3^3 lattice, no plateaux in the effective masses for the A_1^{++}, E^{++} and T_2^{++} channels were observed; the mass in the T_1^{+-} channel was found to be 1.44(1). The operators used in these runs were the same as those constructed for the large volume runs and thus, were not optimized to give large overlaps with the light torelon states present in small volumes. It is likely that this effect was responsible for the poor overlap of our operators with the scalar and tensor states on the 3^3 lattice.

The properties, such as the mass, of a glueball confined in a small box with periodic boundary conditions differ from those in an infinite volume. The modification of the mass of a particle due to finite volume effects has been estimated in Ref. [13]:

$$a_t m_G(z) = a_t m_G(\infty) \left[1 - \lambda_G \exp(-\sqrt{3}z/2)/z\right], \tag{16}$$

where z is the dimensionless length scale $z = m_{A_1^{++}} L_s$, $m_{A_1^{++}}$ is the infinite-volume mass of the scalar glueball, and λ_G is related to the strength of an effective triple scalar glueball interaction vertex. The mass shift given in Eq. 16 is valid for sufficiently large z and arises from the exchange of scalar glueballs across the periodic boundaries of the lattice. Finite volume errors in our glueball masses measured on an 8^3 lattice at $\beta = 2.4$, $\xi = 3$ (where $L_s \approx$ 2 fm, similar to the volumes used in the other nine simulations) can be estimated by fitting the form given in Eq. 16 to the masses in Table XV. Let $\omega = a_t m_{A_1^{++}}$ and $\rho = \xi L_s/a_s$, then $z = \rho\omega$. The A_1^{++} fit was done first using the function $a_t m(z) = \omega - \lambda_{A_1^{++}} \exp(-\sqrt{3}\rho\omega/2)/\rho$, where ω and $\lambda_{A_1^{++}}$ were the fitting parameters. The best fit value for ω was then used in the fits to the results for the other irreps; to simplify matters, the uncertainty in ω was neglected in these fits. The T_1^{+-} fit also included the energy estimate extracted from the $L_s/a_s = 3$ simulation. The results of these fits are summarized in Table XVI; the estimates of the finite volume errors are listed in the final column of this table and are given by $m_G(8\omega\xi)/m_G(\infty) - 1$ using Eq. 16. In all cases, these errors were insignificant compared to statistical errors; this means, for example, that any differences between the large-volume masses in the T_2 and E channels must be due purely to discretization errors. It is interesting to note that our estimate of $\lambda_{A_1^{++}}$ agrees well with the value 190 ± 70 found in Ref. [12].

C. Continuum limit extrapolations

The glueball mass estimates in terms of a_t^{-1} were combined with the determinations of the hadronic scale r_0/a_s. The results are shown in Figs. 12, 13, and 14. In these figures, the dimensionless product of r_0 and the glueball mass estimates are shown as functions of $(a_s/r_0)^2$. Solid symbols indicate results from the $\xi = 3$ simulations, while open symbols are used for the results from the $\xi = 5$ runs. In Fig. 12, the lowest-lying masses in each of the channels A_1^{++}, E^{++}, T_2^{++}, and T_1^{+-} are compared with results from small-a_s Wilson action simulations. The lowest-lying and first-excited masses in the E^{++} and T_2^{++} channels are shown in Fig. 13, and the ground-state and first-excited state in the A_1^{++} channel are depicted in Fig. 14. To extract physical predictions (for the pure-gauge theory), the curves in these plots must be extrapolated to the continuum limit $a_s/r_0 \to 0$. Discretization errors are given by the deviations of the finite-a_s results from these limiting values.

The lowest-lying states in the E^{++} and T_2^{++} channels correspond to the five polarizations of the tensor 2^{++} glueball in the continuum. Differences between the E^{++} and T_2^{++} masses are a measure of violations of rotational symmetry due to finite spacing artifacts. In Fig. 12, such violations are seen to be small for our less coarse lattices and become appreciable as the spacing gets very large. Discretization errors in the T_2^{++} exceed those of the E^{++}; on our coarsest lattices, finite spacing errors are only a few per cent for the E^{++} channel, but about 15% in the T_2^{++} channel. In the E^{++} channel, the $\xi = 3$ results differ very little from those using the higher aspect ratio $\xi = 5$, suggesting that the $O(a_t^2)$ errors are negligible. However, small differences between the results from the two anisotropies are visible in the T_2^{++} channel. One expects that $O(a_t^2)$ errors will decrease as ξ is increased. Since the T_2^{++} discretization errors are slightly larger for the $\xi = 5$ runs, $O(a_t^2)$ errors can account for this difference only if such errors offset the $O(a_s^4)$ errors.

The leading discretization errors in the tensor glueball masses are expected to be $O(a_t^2, a_s^4, \alpha_s a_s^2)$. However, we have already argued that the results in Fig. 12 imply that the $O(a_t^2)$ errors are negligible. Since the action included mean-field correction factors, we also expected that $O(a_s^4)$ errors would dominate over $O(\alpha_s a_s^2)$ errors and in our continuum limit extrapolations, we assumed that this was true unless the fit provided compelling evidence to the contrary. Although we expected the leading discretization errors to be $O(a_s^4)$, the following three functions were used in our continuum limit extrapolations:

$$\varphi_0(a_s) = r_0 m_G, \tag{17}$$
$$\varphi_2(a_s) = r_0 m_G + c_2\ (a_s/r_0)^2, \tag{18}$$
$$\varphi_4(a_s) = r_0 m_G + c_4\ (a_s/r_0)^4, \tag{19}$$

where c_2, c_4 and $r_0 m_G$ are best-fit parameters. The results of these fits are given in Table XVII for the $\xi = 3$ data and Table XVIII for the $\xi = 5$ simulations. Comparing the values of χ^2/dof, one sees that the fitting function φ_4 was preferred for both the $\xi = 3$ and $\xi = 5$ results, although only marginally so for $\xi = 3$. Given this fact and our expectation that φ_4 should best describe the leading discretization effects, we took $r_0 m_G$ from the φ_4 fits as our continuum limit estimates (indicated in boldface in Tables XVII and XVIII). These four estimates are in very good agreement not only with one another, but also with the Wilson action estimates. These fits using φ_4 are shown in Fig. 12. For our final estimate of the tensor glueball mass, we performed a simultaneous fit with the four data sets (two irreps and two anisotropies) using four separate φ_4 functions but constraining the intercept parameter $r_0 m_G$ to be the same for all four fitting functions. This yielded $r_0 m(2^{++}) = 5.85 \pm 0.02$ with $\chi^2/\text{dof} = 1.01$, in agreement with the Wilson action estimate $r_0 m(2^{++}) = 6.0 \pm 0.1$, obtained by fitting all of the Wilson action measurements shown in Fig. 12 to φ_0.

We also examined the discretization errors in the masses of the first-excited glueball states in the E^{++} and T_2^{++} channels. These are shown in Fig. 13. There are several reasons for interpreting these data as different polarizations of a spin-two excited state:

the two irreps extrapolate to the same continuum limit value; if the T_2^{++} state were spin three, then there would be a degeneracy with the T_1^{++} and A_2^{++} channels and this was not observed (these results will be presented elsewhere); if they were polarizations of a spin-four state, then again, a similar level must also be found in the T_1^{++} channel. The degeneracy between the two irreps and the weak finite-volume dependence of their energies also makes an interpretation of this state as a torelon pair or a two-scalar-glueball scattering state unlikely, although the mass of this level lies close to twice the mass of the scalar glueball. Continuum limit extrapolations were performed using the three functions of Eqs. 17-19; measurements from the two largest a_s spacings for $\xi = 3$ and the single largest spacing for $\xi = 5$ were excluded from these fits. The results are given in Tables XVII and XVIII. Again, we expected φ_4 to provide the most reliable extrapolations to the $a_s \to 0$ limit; this was confirmed by the fact that φ_4 yielded E^{++} and T_2^{++} continuum limits in best agreement with each other. Differences found between the $\xi = 3$ and $\xi = 5$ extrapolations were not statistically significant. The fits using φ_4 are shown in Fig. 13. Our final determination of the mass of the excited tensor glueball, obtained from a constrained set of four φ_4, similar to the ground-state extraction, was $r_0 m(2^{*++}) = 8.11 \pm 0.04$, where $\chi^2/\mathrm{dof} = 2.3$. This mass has not been reliably determined in any previous simulations.

Finite spacing errors in the mass of the T_1^{+-} pseudovector glueball were also studied. These were found to be small and are shown in Fig. 12. The results from the different anisotropies are in good agreement. Extrapolations to the $a_s \to 0$ limit were done using the three functions φ_0, φ_2, and φ_4; the results of these fits are summarized in Tables XVII and XVIII. The continuum limits obtained from fits to the $\xi = 3$ and $\xi = 5$ data agreed only for the constant fit form φ_0. The fits to φ_2 and φ_4 yielded slope parameters (c_2 and c_4) with large relative errors and opposite signs for the different anisotropies. Hence, the function φ_0 was used to extrapolate to the continuum limit. Due to the very good agreement between the $\xi = 3$ and $\xi = 5$ results, all ten data points were used in our extrapolation fit. Our estimate from this fit (shown in Fig. 12) was $r_0 m(1^{+-}) = 7.21 \pm 0.02$, where $\chi^2/\mathrm{dof} = 1.55$, in agreement with the extrapolation $r_0 m(1^{+-}) = 7.5 \pm 0.4$ using φ_0 of the Wilson action results shown in Fig. 12.

In contrast to the tensor and pseudovector, the scalar glueball mass showed significant finite spacing errors (see Fig. 12), even for our less coarse lattices. As a_s was increased, the scalar mass first decreased, reached a minimum near $a_s/r_0 \sim 0.6$, then gradually increased. Near the minimum, the mass was about 25% lower than estimates of the continuum limit from small-a_s Wilson action computations; a 20% discretization error was observed in the result from our smallest a_s simulation. Although the magnitudes of these errors were significant, they were smaller than those obtained using the Wilson action by a factor of two. In order to extrapolate to the continuum limit, an appropriate fitting function was needed. The leading discretization errors were expected to be $O(a_t^2, a_s^4, \alpha_s a_s^2)$. However, there were no distinguishable differences between the $\xi = 3$ and $\xi = 5$ results, suggesting that the $O(a_t^2)$ errors were negligible, leaving us to consider $O(a_s^4, \alpha_s a_s^2)$ effects. By inspection, one sees that the fitting form φ_4, which neglects one-loop $O(\alpha_s a_s^2)$ effects, cannot describe the data, in contrast to the data for the tensor and pseudovector glueballs. As $a_s \to 0$, we expect the coupling $\alpha_s(a_s)$ to vanish as $-1/\ln(a_s\Lambda)$, where Λ is an appropriate scale parameter. Hence, we were led to consider the following four-parameter fitting function:

$$\varphi_{1L}(a_s) = r_0 m_G + c_2 \; \frac{(a_s/r_0)^2}{c_L - \ln\left[(a_s/r_0)^2\right]} + c_4 \; (a_s/r_0)^4. \tag{20}$$

However, it was not known how reliably the leading perturbative behavior of $\alpha_s(a_s)$ would describe the true cut-off dependence of the coupling over the large range of spacings considered. Taking this into account and inspecting the behavior of the actual data, we decided to also consider the following simpler quadratic form:

$$\varphi_{2,4}(a_s) = r_0 m_G + c_2 \; (a_s/r_0)^2 + c_4 \; (a_s/r_0)^4. \tag{21}$$

Both of these functions were fit to the mass measurements from all ten simulations; the results of these fits are summarized in Table XIX. The function φ_{1L} yielded a slightly better fit and a continuum limit for the scalar glueball mass of 3.98 ± 0.15. This fit is shown in Fig. 12. An extrapolation of existing Wilson action data using φ_2 yielded 4.33 ± 0.05. Given the quality of the scalar glueball mass estimates using the Wilson action, this slight discrepancy raises doubts concerning the reliability of the extrapolation using φ_{1L}; mass estimates using the improved action for a few values of a_s smaller than those considered here would be needed to resolve this discrepancy.

One explanation for the 20% discretization errors in the scalar glueball mass is that the scalar glueball is extremely small. However, there is evidence[14, 15] that the presence of a critical endpoint of a line of phase transitions (not corresponding to any physical transition found in QCD) in the fundamental-adjoint coupling plane is responsible for lowering the scalar glueball mass near the crossover region in the Wilson action. It is possible that the scalar glueball mass in the improved action used here may be similarly influenced. If so, the fact that this effect appears to be less pronounced for this action suggests the possible existence of other perturbatively-improved actions in which the scalar glueball mass is even less affected by scaling violations. We are currently searching for such actions.

Discretization errors in the mass of the first-excited state in the A_1^{++} channel were also found to be significant, as shown in Fig. 14. The mass of this state is nearly twice that of the lowest-lying scalar glueball, suggesting that this state may simply be two glueballs. Given the significant discretization errors in the single glueball scaling data, one would expect similar systematic errors in the two glueball state. The absence of any level of similar mass in all other channels justifies the spin-zero interpretation of this state. Considering the difficulties encountered in extrapolating the lowest-lying scalar to the continuum limit, we made no serious attempt to determine the continuum limit of this first-excited state. However, the result of a fit using $\varphi_{2,4}$ is included in Table XIX. The possible interpretation of this level as a two glueball system might be strengthened by a more precise finite-volume study.

D. Conversion to physical units

In order to convert our glueball mass computations into physical units, we must specify the value of the hadronic scale. The hadronic scale r_0 has a precise definition in terms of the static-quark potential. However, the static-quark potential cannot be directly measured in an experiment; it must be deduced indirectly from other observables. We decided to use a variety of different physical quantities to deduce r_0.

In Table XX, estimates of r_0^{-1} using the results from various quenched lattice simulations are shown. For each computation, the quantity used to set the lattice spacing, such as the mass of the ρ or the $1P-1S$ splitting in heavy quarkonia, is indicated. The determination of r_0^{-1} from a^{-1} was accomplished using values of a/r_0 given in Ref. [16] for the Wilson gluonic action at various values of β, interpolating where necessary. Note that due to quenching effects, r_0 varies with the quantity used to set the scale. The entries in the last column of Table XX cannot be considered as different measurements of a single quantity and thus, strictly speaking, their weighted average has no statistical meaning. The last column of the table is meant to illustrate the range of values one obtains for r_0^{-1} when using various scale setting quantities. We expect that the value of r_0^{-1} appropriate for the low-lying glueballs should lie somewhere within this range. The simple average $r_0^{-1} = 410 \pm 20$ MeV of the determinations in Table XX was taken as our estimate of the hadronic scale.

For our final continuum mass estimates of the tensor glueball, we found $2400 \pm 10 \pm 120$ MeV (where the first error is statistical and the second is from uncertainties in the determination of r_0). It is interesting to note that our mass estimate lies within 8% of the mass of the $f_J(2220)$ resonance [17, 18], reported to have quantum numbers (even)$^{++}$. In order to make a direct comparison with experiment, however, corrections to our result from light quark effects and mixings with nearby conventional mesons must be taken into account. Our estimate of the mass of the first-excited glueball in the tensor channel was $3320 \pm 20 \pm 160$ MeV; for the pseudovector state, we found a mass of $2960 \pm 10 \pm 140$ MeV. Our estimate from the fit using φ_{1L} for the mass of the scalar glueball was $1630 \pm 60 \pm 80$ MeV; however, we regard the continuum limit extrapolation for this state as being less reliable than those for the other glueballs.

E. Comparison of efficiencies

A quantitative comparison of efficiencies is difficult to make. There are many factors which affect the overall efficiency of a Monte Carlo simulation. Certainly, the number of link updates is an important factor. The speed of an update is, of course, platform-, action-, and algorithm-dependent. On the DEC Alpha-workstations we used, a CM update using an improved action required twice as much time as for the Wilson action; the improved-action OR updating time was three times longer. Critical slowing down and thermalization are also contributing factors, but a crucial issue is the reduction of excited-state contaminations in the glueball correlators. In our coarse lattice simulations, we found that current methods for constructing good glueball operators were very effective in hastening the onset of plateaux in the effective masses.

Given these difficulties in assessing the efficiency of a glueball simulation, we decided to make our comparisons based simply on the number of link updates N_{lu} and the fractional error ϵ attained in the final mass estimates. Since the error in a Monte Carlo estimate decreases with the number of measurements N as $1/\sqrt{N}$, we expect that the reciprocal product of the number of link updates and the square of the fractional error is approximately proportional to the efficiency of a simulation; we denote this quantity by $\mathcal{E} = 1/(\epsilon^2 N_{lu})$. An interesting comparison to make is between simulations at a small lattice spacing, such as $a_s \sim 0.05$ fm, using the Wilson action and improved-action simulations at a spacing $a_s \sim 0.2$ fm. Such a comparison is relevant because the discretization errors in these cases are of comparable magnitude, excepting the scalar glueball mass. For the $\beta = 6.4$ Wilson action run in Ref. [19] by the GF11 collaboration using gauge invariant glueball operators, a total of 3.13×10^{12} link updates were performed, an error of 2.5% was achieved in the scalar glueball mass, and a fractional error of 3.6% was obtained for the tensor mass. Using $r_0 = 0.48$ fm and $a_s/r_0 = 0.101(2)$, the lattice volume in this simulation was $(1.55\text{ fm})^2 \times (1.45\text{ fm})$. For the same value of β in Ref. [20] by the UKQCD collaboration, 1.35×10^{11} link updates were made and fractional errors 3.4%, 3.3%, and 9% were obtained for the scalar, tensor, and pseudovector masses, respectively. The lattice volume was $(1.55\text{ fm})^3$ for this simulation. In our $\beta = 2.6$, $\xi = 3$ run, 5.76×10^9 link updates were performed and 1.5%, 1.0%, and 1.0% errors in the scalar, tensor, and pseudovector masses were achieved. Our lattice volume was $(1.93\text{ fm})^3$ since $a_s/r_0 = 0.4021(9)$. For our $\beta = 2.4$, $\xi = 5$ run, the number of link updates was 9.83×10^9 and the errors obtained in the scalar, tensor, and pseudovector masses were 1.0%, 0.5%, and 0.8%, respectively. Using $a_s/r_0 = 0.459(1)$, our lattice volume for this run was $(1.76\text{ fm})^3$. Thus, the ratios of the $\mathcal{E}$ values for our $\beta = 2.6$ and $\beta = 2.4$ simulations to those of the GF11 run were 1500 and 2000, respectively, for the scalar glueball mass, and 7000 and 17000 for the tensor glueball mass. The ratios of the $\beta = 2.6$ and $\beta = 2.4$ $\mathcal{E}$-values to those of the UKQCD run were 120 and 160, respectively, for the scalar mass, 260 and 600 for the tensor, and 1900 and 1700 for the pseudovector.

Considering our ten simulations together, a total of 5×10^{10} link updates were performed. For the Wilson action simulations of Refs. [19, 20], an estimated 10^{13} and 10^{12} link updates were required, respectively, to generate continuum limit results whose statistical uncertainties were larger (for the tensor and pseudovector states) than those quoted here: the statistical error on our estimate for $r_0 m(2^{++})$ was about five times smaller than that from the extrapolation of the Wilson action results, and for $r_0 m(1^{+-})$, the uncertainty was twenty times smaller, implying that about $25-400$ times greater statistics would be required for similar accuracy. Thus, in total, the anisotropic lattice simulations were certainly more than 1000 times more efficient.

The above discussion illustrates the computational advantages of extracting non-scalar glueball masses from simulations on coarse, anisotropic lattices ($a_s \sim 0.2$ fm) using an improved action instead of lattices for which $a_s \sim 0.05$ fm. The excellent overlaps achieved from our variational calculations demonstrate another advantage of simulating on coarse spatial lattices. The glueball wavefunctions extend over only a few points of the lattice when $a_s \approx 0.2$ fm. Thus, variational calculations using a feasible number of basis functions (a dozen or so) can yield very good approximations to the glueball wavefunctions. This will be especially important for future decay constant calculations and determinations of mixings with non-glueball states. These advantages have already enabled us to study the more massive glueball states which have yet to be simulated reliably using the Wilson action; these results will be reported elsewhere.

These advantages are less clear for the scalar glueball mass due to the presence of 20% discretization errors at $a_s \sim 0.2$ fm. Using the action of Eq. 1, simulations at one or more lattice spacings smaller than 0.2 fm would be needed to firmly establish the continuum limit. A more attractive approach would be to use an action for which discretization errors in the scalar glueball mass at $a_s \sim 0.2$ fm are negligibly small. The search for such an action is currently underway.

VI. CONCLUSION

We have demonstrated the advantages of using anisotropic lattices and an improved gluonic action for simulating glueballs. Ten simulations at lattice spacings ranging from 0.2 to 0.4 fm were performed using DEC Alpha-workstations, and the results were extrapolated to the continuum limit. Results for the masses of the scalar (0^{++}), the tensor (2^{++}), and the pseudovector (1^{+-}) glueballs in $SU(3)$ pure-gauge theory were presented in terms of the hadronic scale r_0^{-1}. The continuum limits for the tensor and pseudovector glueball masses were obtained with uncertainties of less than 1%, significantly improving upon previous estimates from Wilson action simulations carried out with the aid of super-computer resources. Extrapolation of the scalar glueball mass to the continuum limit was hampered by uncertainties in choosing the fitting function and discretization errors which were $20-25\%$ even for our smallest lattice spacings; although uncomfortably large, these finite-spacing errors were half as large as those obtained using the Wilson action. Finite volume errors in our results were shown to be negligible. The masses of the first excited states in the scalar and tensor channels were also examined.

Our results show that spatially-coarse, anisotropic lattice simulations are an effective means of studying gluonic systems. The techniques exploited here are sufficiently powerful to overcome the difficulties which plague Monte Carlo calculations involving gluonic excitations. These methods should be useful for studying the spectrum of heavier glueball states. Data for the masses of all twenty lattice irreps of the cubic group (including parity and charge conjugation) are currently being accumulated in order to survey the spectrum of $SU(3)$ glueball states below 4 GeV comprehensively. We shall report on these results in the near future. We also plan to use the techniques outlined in this paper to determine various glueball matrix elements and decay strengths, to investigate the mixings of glueballs with conventional hadronic states, and to study mesonic states containing excited glue (the so-called hybrid mesons). The size of discretization errors in the scalar glueball mass was the only disappointing aspect of this work; we are currently investigating a new class of lattice actions with the hope of reducing these lattice artifacts for $a_s \sim 0.2$ fm to the level of a few per cent.

VII. ACKNOWLEDGMENTS

We would like to thank Peter Lepage, Julius Kuti, Chris Michael, Terrence Draper, and Keh-Fei Liu for helpful discussions. This work was supported by the U.S. DOE, Grant No. DE-FG03-90ER40546. MP is grateful to the University of Kentucky Center for Computational Sciences for financial support.

REFERENCES

[1] C. Morningstar and M. Peardon, Nucl. Phys. B (Proc. Suppl.) **47**, 258 (1996).
[2] C. Morningstar, Nucl. Phys. B (Proc. Suppl.) **53**, 914 (1996).
[3] C. Morningstar and M. Peardon, Nucl. Phys. B (Proc. Suppl.) **53**, 917 (1997).
[4] M. Alford *et al.,* in preparation.
[5] F. Brandstaeter, A. Kronfeld, and G. Schierholz, Nucl. Phys. **B345**, 709 (1990).
[6] M. Albanese *et al.,* Phys. Lett. B **192**, 163 (1987).
[7] M. Teper, Phys. Lett. B **183**, 345 (1986).
[8] Y. Liang *et al.*, Phys. Lett. B **307**, 375 (1993).
[9] B. Berg and A. Billoire, Nucl. Phys. **B221**, 109 (1983).
[10] R. Sommer, Nucl. Phys. **B411**, 839 (1994).
[11] G. Parisi *et al.*, Phys. Lett. **128B**, 418 (1983).
[12] G. Schierholz, Nucl. Phys. B (Proc. Suppl.) **9**, 244 (1989).
[13] M. Lüscher, Commun. Math. Phys. **104**, 177 (1986).
[14] U. Heller, Phys. Lett. B **362**, 123 (1995).
[15] A. Patel *et al.,* Phys. Rev. Lett. **57**, 1288 (1986).
[16] G.S. Bali and K.S. Schilling, Int. J. Mod. Phys. **C4**, 1167 (1993) and private communication; H. Wittig, Nucl. Phys. B (Proc. Suppl.) **42**, 288 (1995).
[17] R.M. Barnett *et al.*, Phys. Rev. D **54**, 1 (1996).
[18] R.M. Baltrusaitis *et al.,* Phys. Rev. Lett. **56**, 107 (1986).
[19] H. Chen *et al.*, Nucl. Phys. B (Proc. Suppl.) **34**, 357 (1994).
[20] G.S. Bali *et al.*, Phys. Lett. B **309**, 378 (1993).
[21] P. de Forcrand and K-F. Liu, Phys. Rev. Lett. **69**, 245 (1992).
[22] C. Michael and M. Teper, Nucl. Phys. **B314**, 347 (1989).
[23] P. de Forcrand *et al.*, Phys. Lett. **160B**, 137 (1985).
[24] C. Davies *et al.,* Phys. Rev. D **50**, 6963 (1994).
[25] C. Davies *et al.,* Phys. Rev. D **52**, 6519 (1995).
[26] T. Bhattacharya *et al.,* Phys. Rev. D **53**, 6486 (1996).
[27] F. Butler *et al.,* Nucl. Phys. **B430**, 179 (1994).
[28] S. Aoki *et al.,* Nucl. Phys. B (Proc. Suppl.) **53**, 355 (1997).
[29] S. Aoki *et al.,* Nucl. Phys. B (Proc. Suppl.) **53**, 349 (1997).
[30] A.X. El-Khadra, Nucl. Phys. B (Proc. Suppl.) **34**, 141 (1994).
[31] C. Bernard, J. Labrenz, and A. Soni, Phys. Rev. D **49**, 2536 (1994).
[32] C.R. Allton *et al.,* Phys. Lett. B **284**, 377 (1992).

FIGURES

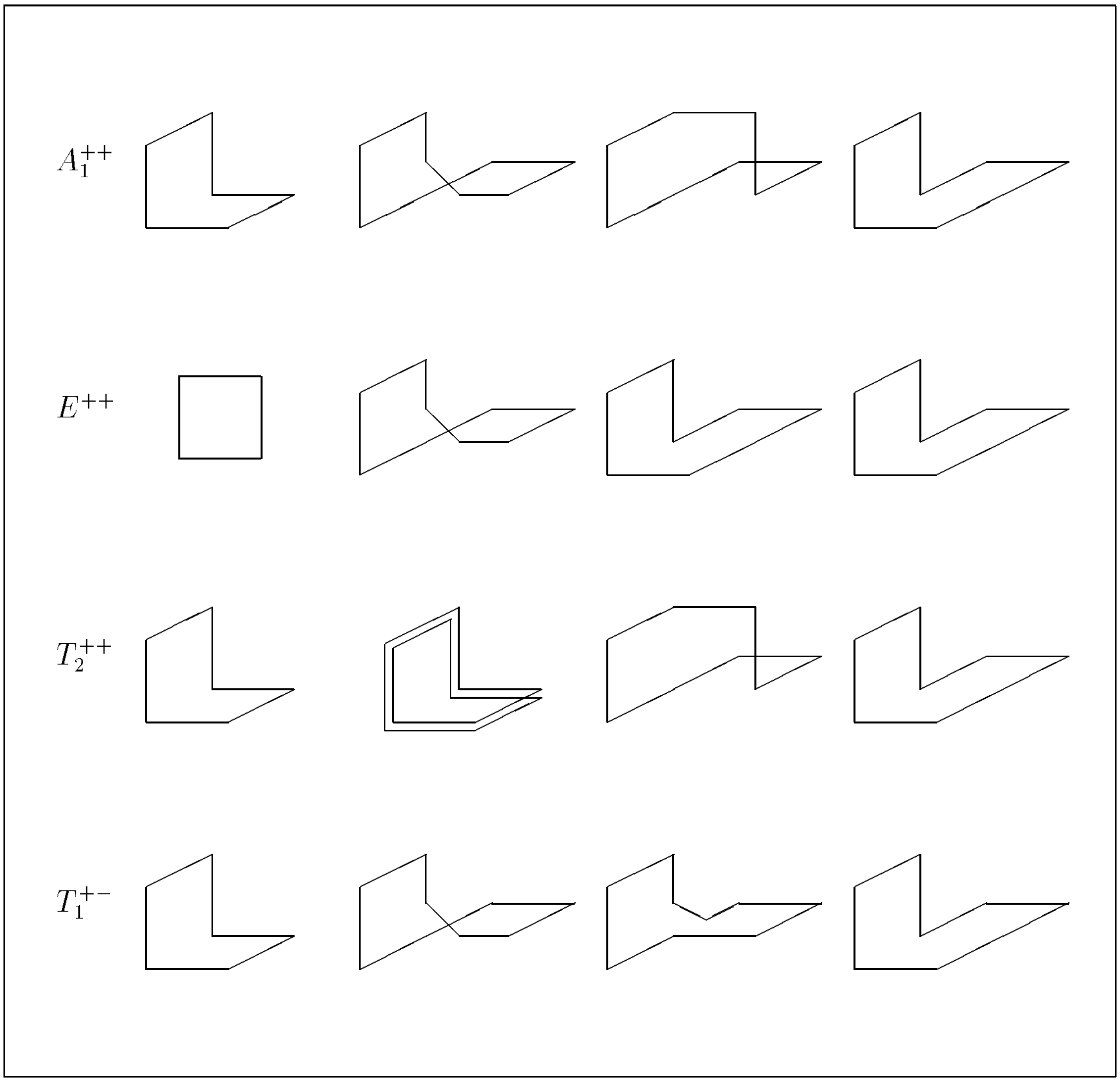

FIG. 1. The four Wilson loop shapes in each channel used to form the lattice glueball operators. The complete set of 24 operators was formed by computing linear combinations of each of these loops rotated and translated across the lattice on six different sets of smoothed links. Where a loop shape occurs twice, it is used in two different projections into the appropriate irreducible representation.

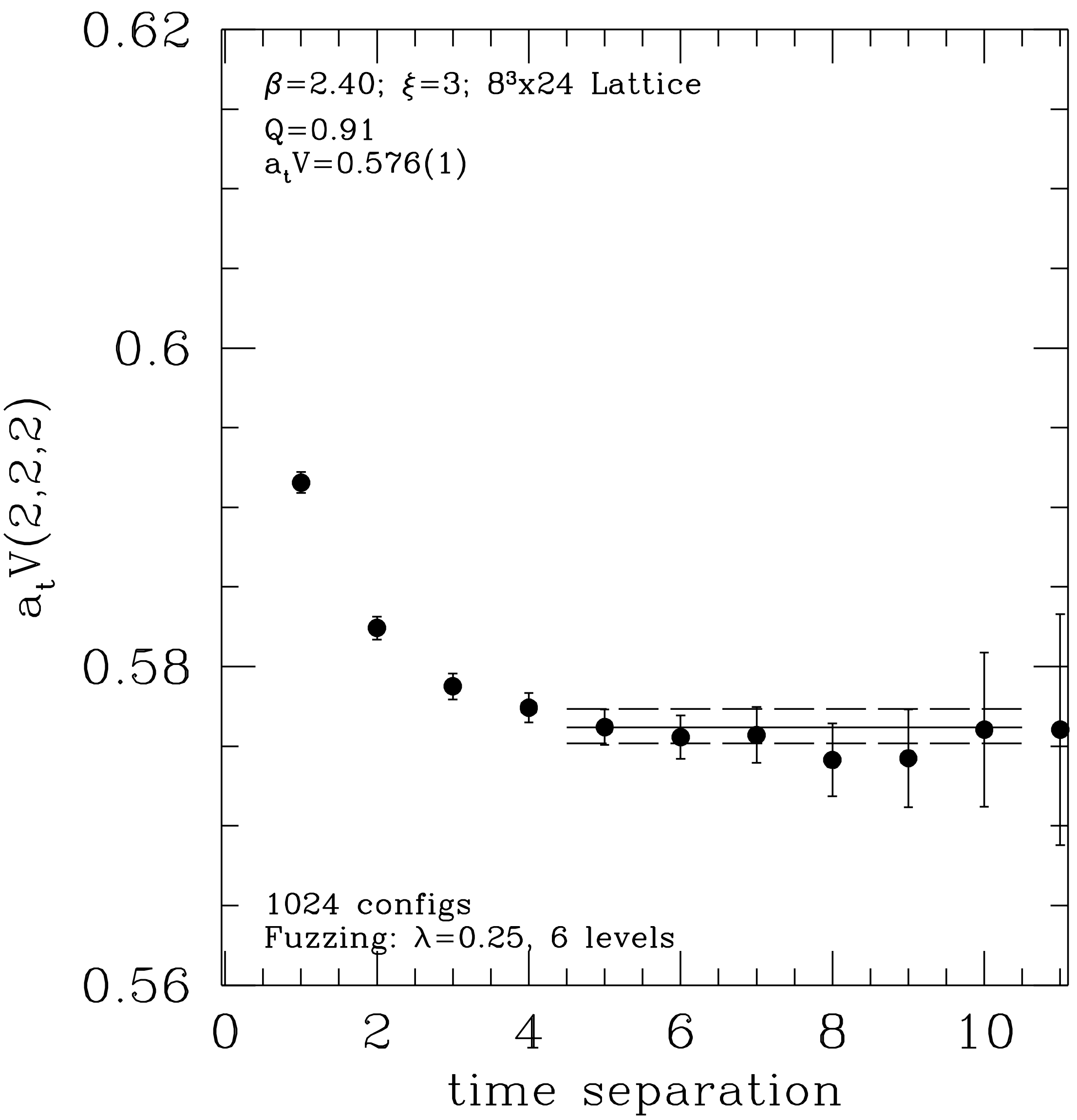

FIG. 2. Effective mass plot showing the results of a single-exponential fit to the Wilson loop for $V(\vec{r})$ with $\vec{r}/a_s = (2,2,2)$, $\beta = 2.4$, and $\xi = 3$. The $t_{\min} - t_{\max}$ region of the fit is also indicated.

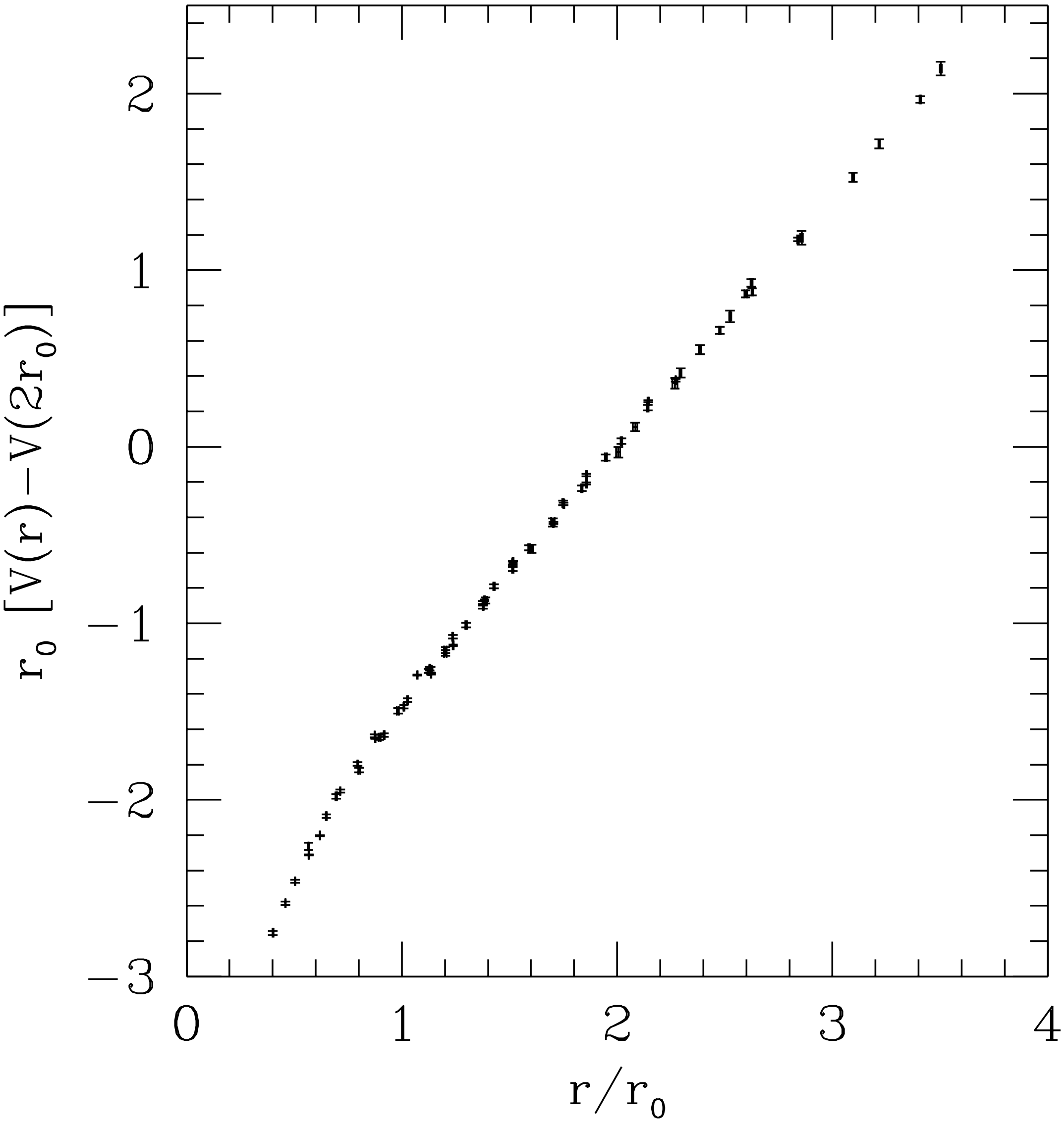

FIG. 3. The static-quark potential $V(\vec{r})$ expressed in terms of the hadronic scale r_0. This plot includes measurements from the $\beta = 2.2$, 2.4, and 2.6 simulations for $\xi = 3$, and the $\beta = 2.2$ and 2.4 simulations for $\xi = 5$. Lattice spacing errors are seen to be small.

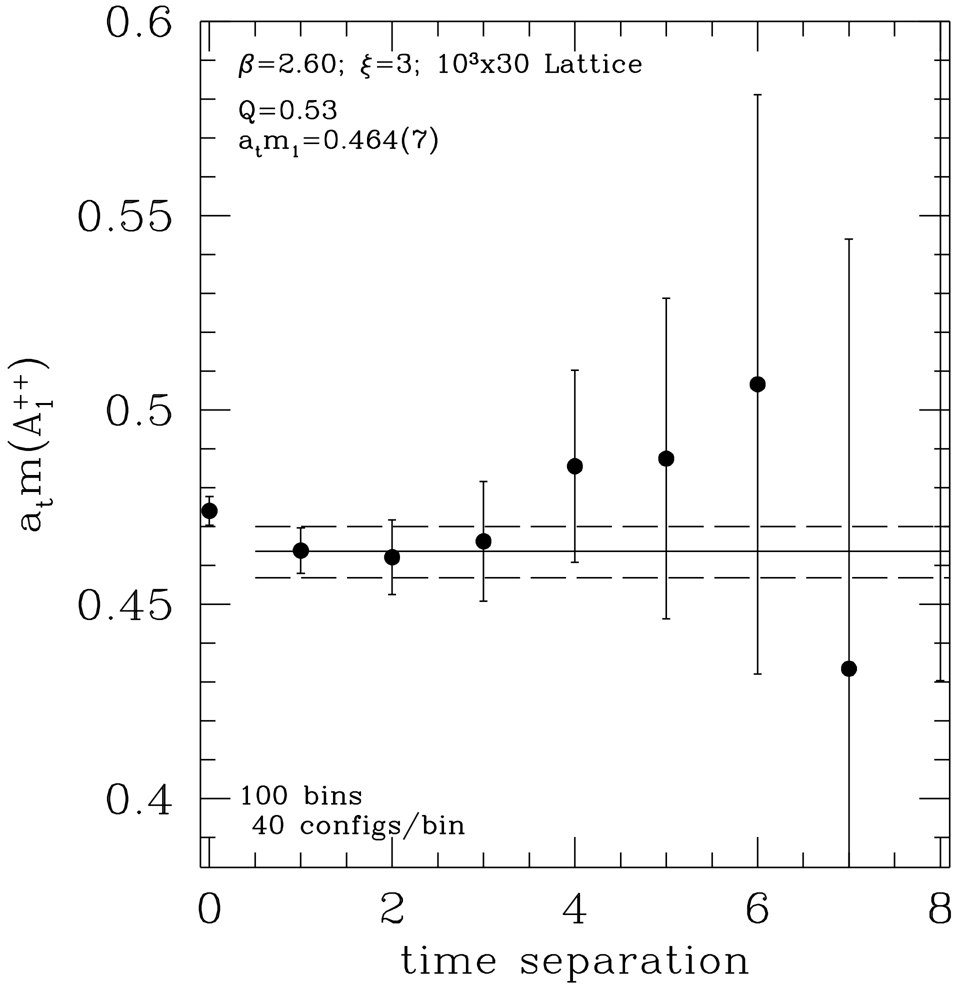

FIG. 4. Effective mass plot showing the results of a single-exponential fit to the glueball correlation function for the A_1^{++} channel for $\beta = 2.6$ and $\xi = 3$. The $t_{\min} - t_{\max}$ region of the fit is also indicated.

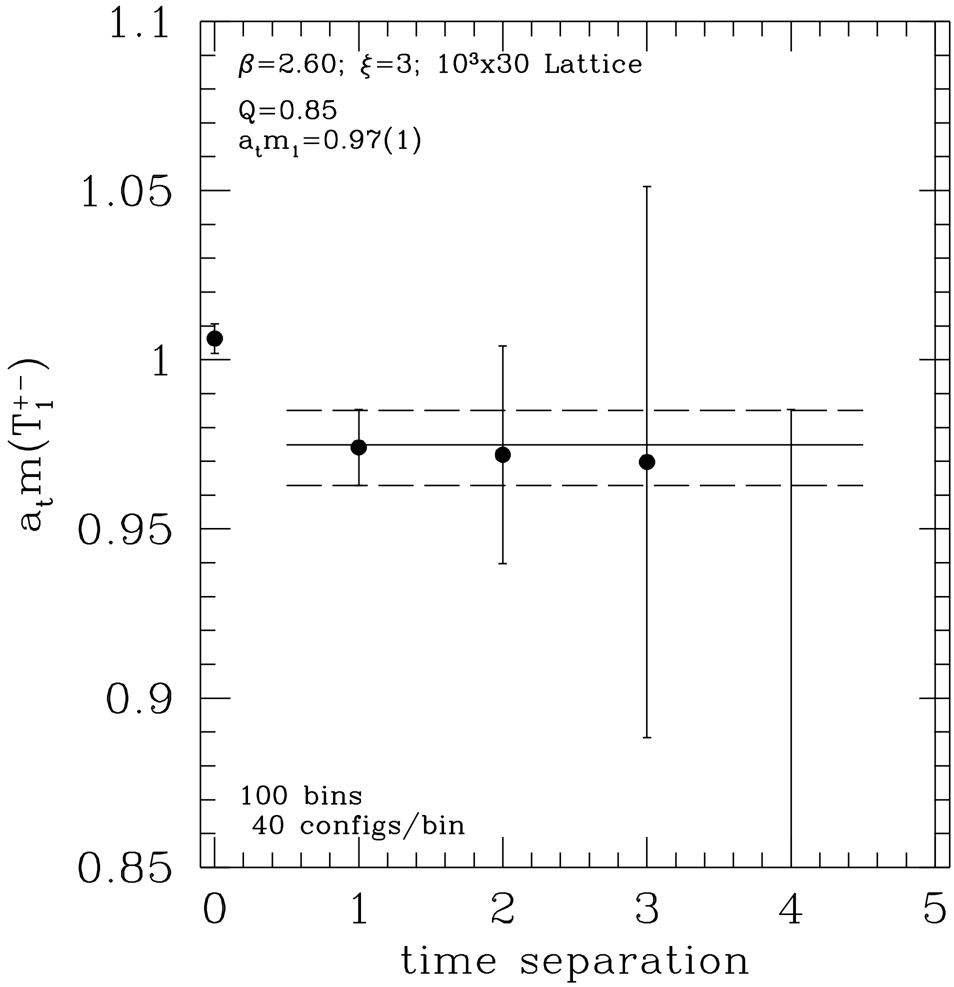

FIG. 5. Effective mass plot showing the results of a single-exponential fit to the glueball correlation function for the T_1^{+-} channel for $\beta = 2.6$ and $\xi = 3$.

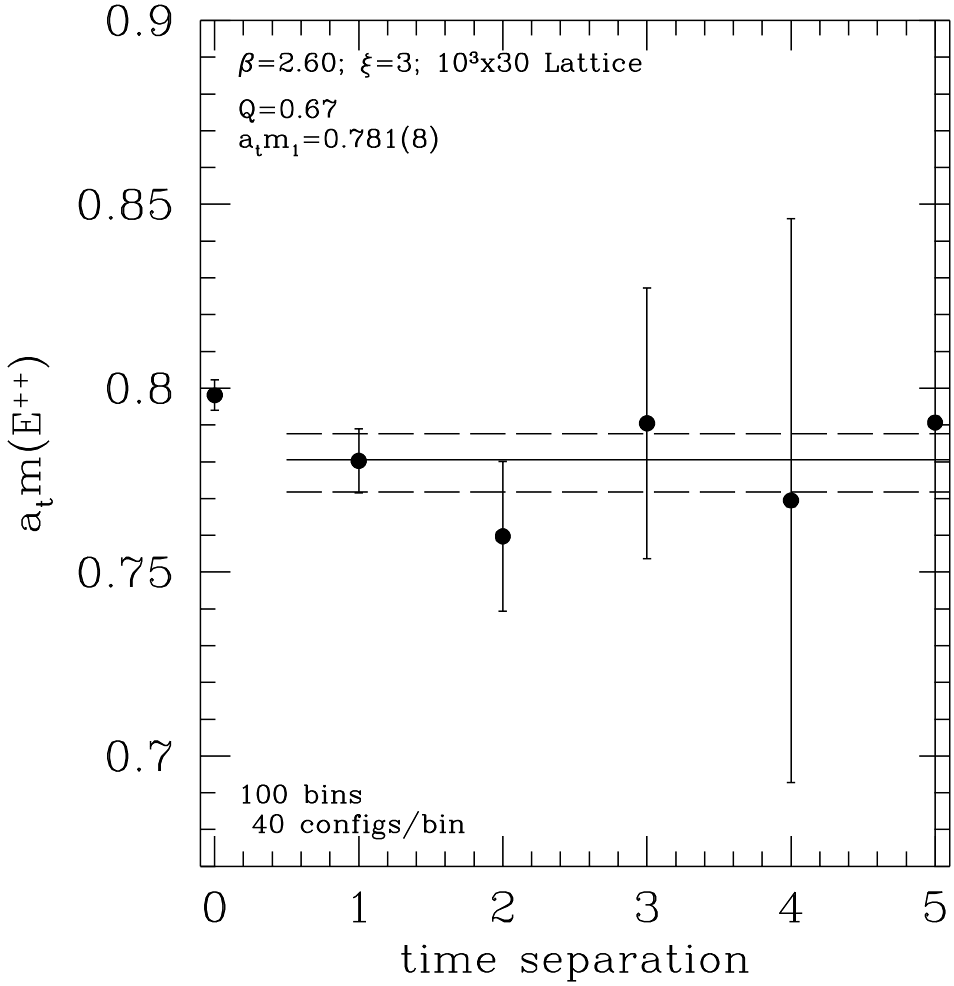

FIG. 6. Effective mass plot showing the results of a single-exponential fit to the glueball correlation function for the E^{++} channel for $\beta = 2.6$ and $\xi = 3$.

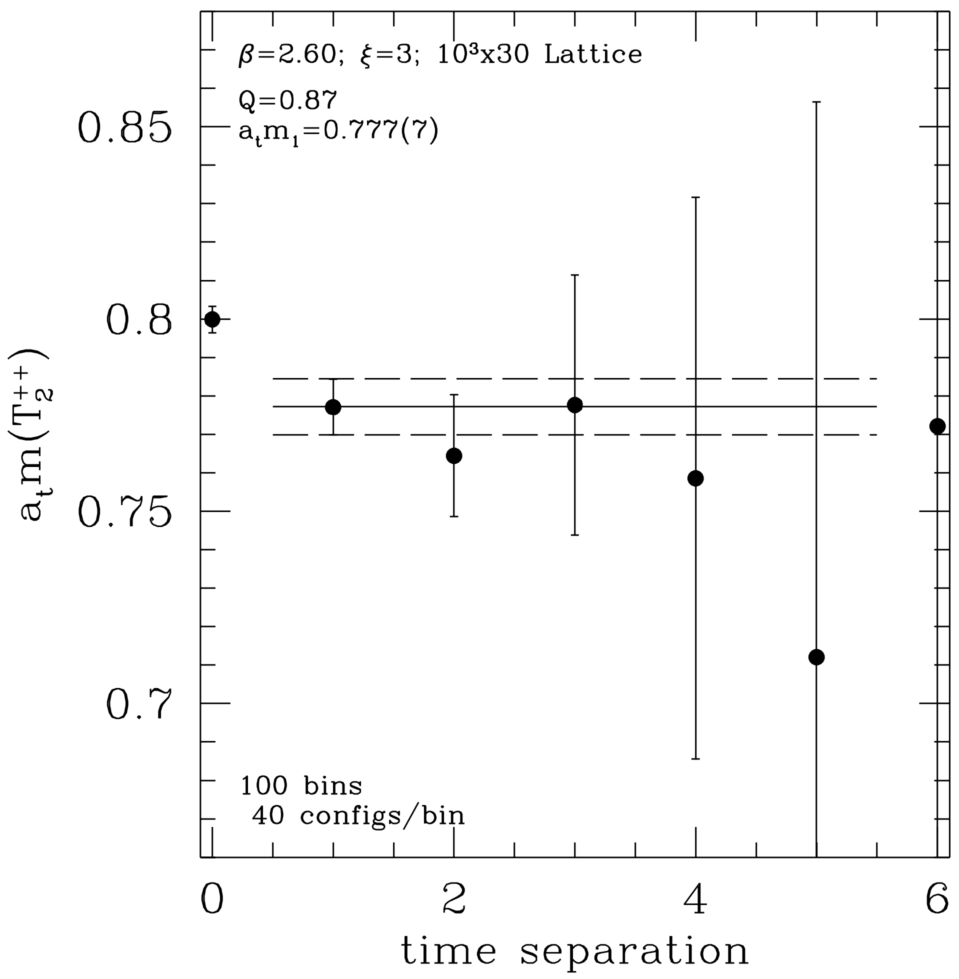

FIG. 7. Effective mass plot showing the results of a single-exponential fit to the glueball correlation function for the T_2^{++} channel for $\beta = 2.6$ and $\xi = 3$.

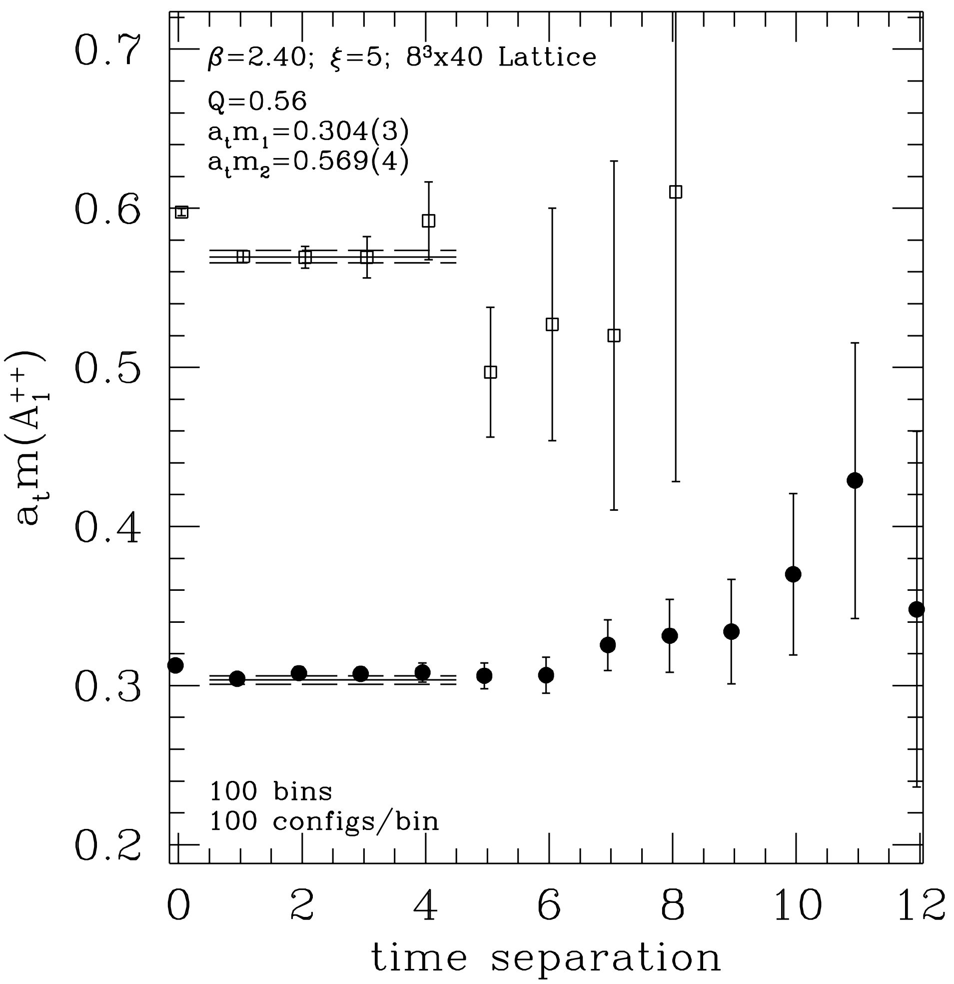

FIG. 8. Effective mass plot showing the results of a two-exponential fit to the 2×2 matrix of glueball correlation functions for the A_1^{++} channel for $\beta = 2.4$ and $\xi = 5$. The $t_{\rm min} - t_{\rm max}$ region of the fit is also indicated.

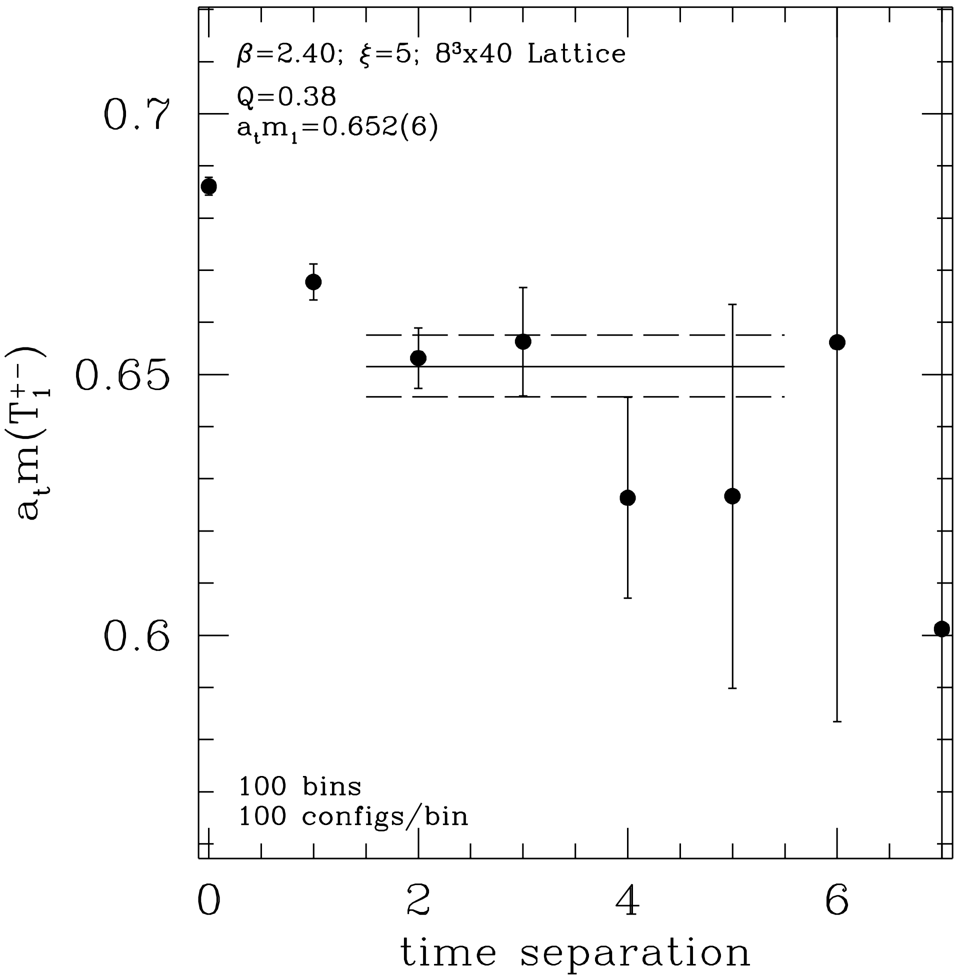

FIG. 9. Effective mass plot showing the results of a single-exponential fit to the glueball correlation function for the T_1^{+-} channel for $\beta = 2.4$ and $\xi = 5$.

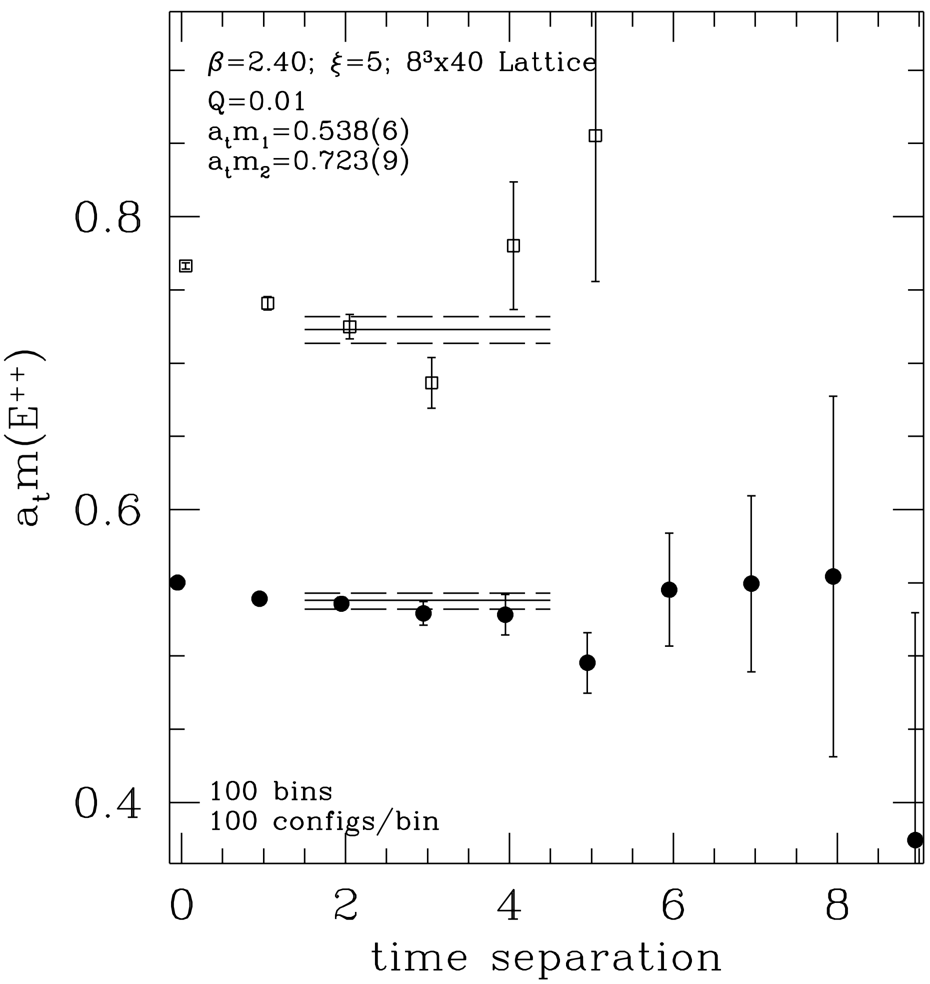

FIG. 10. Effective mass plot showing the results of a two-exponential fit to the 2×2 matrix of glueball correlation functions for the E^{++} channel for $\beta = 2.4$ and $\xi = 5$. The $t_{\mathrm{min}} - t_{\mathrm{max}}$ region of the fit is also indicated.

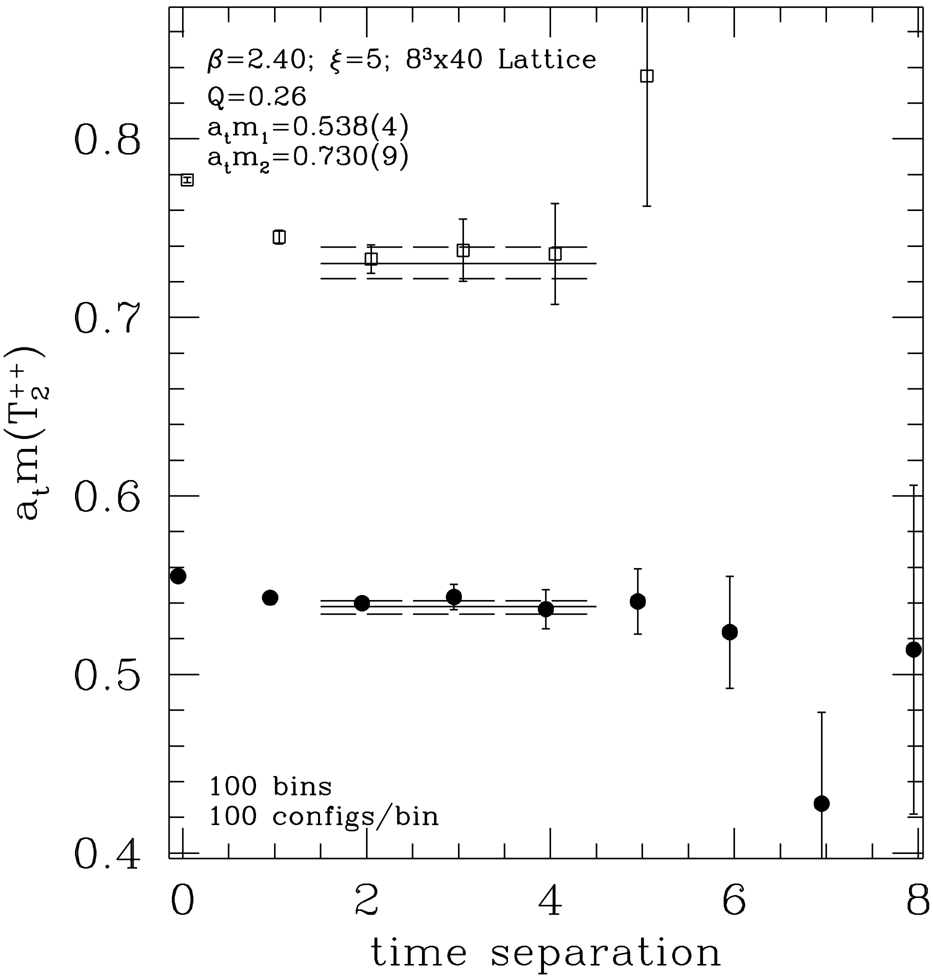

FIG. 11. Effective mass plot showing the results of a two-exponential fit to the 2×2 matrix of glueball correlation functions for the T_2^{++} channel for $\beta = 2.4$ and $\xi = 5$. The $t_{\min} - t_{\max}$ region of the fit is also indicated.

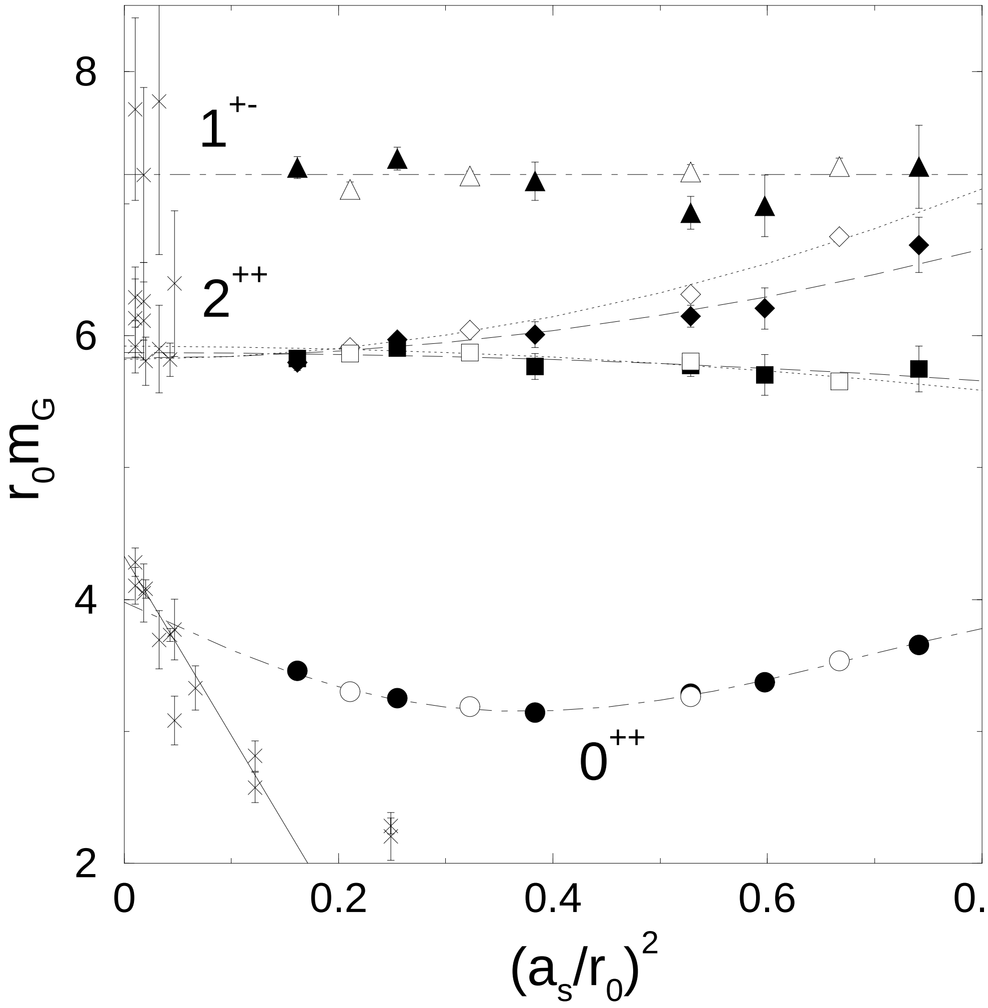

FIG. 12. Glueball mass estimates in terms of r_0 against the lattice spacing $(a_s/r_0)^2$. Results from the $\xi = 5$ simulations for the lattice irreps A_1^{++}, E^{++}, T_2^{++} and T_1^{+-} are labeled $\circ$, $\Box$, $\Diamond$, and $\triangle$, respectively. The corresponding solid symbols indicate the results from the $\xi = 3$ simulations. Data from Wilson action simulations taken from Refs. [19, 22, 20, 23] are shown using crosses. The dashed, dotted, and dash-dotted curves indicate extrapolations to the continuum limit obtained by fitting to the $\xi = 3$ data, the $\xi = 5$ data, and all data, respectively. The solid line indicates the extrapolation of the Wilson action data to the continuum limit.

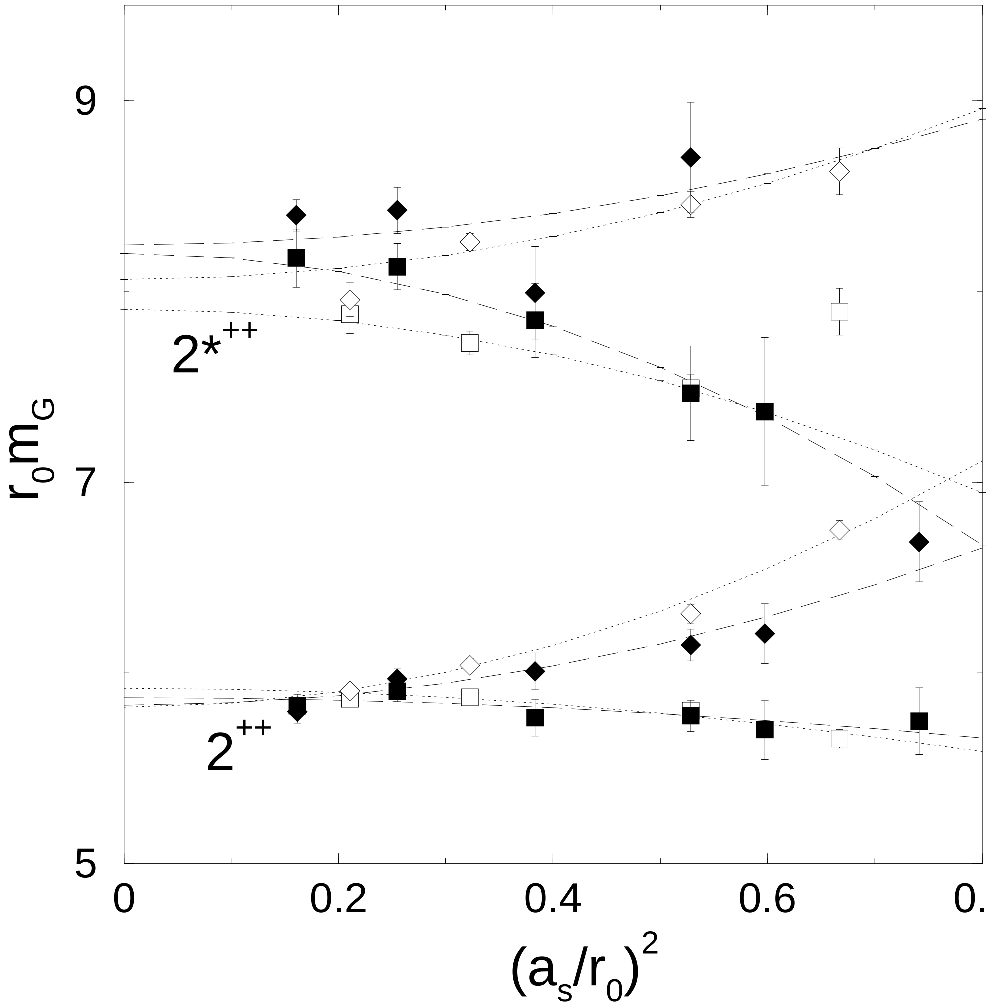

FIG. 13. Estimates of the masses of the tensor glueball and its first-excited state in terms of r_0 against the lattice spacing $(a_s/r_0)^2$. Results from the $\xi = 5$ simulations for the E^{++} and T_2^{++} irreps are labeled by $\Box$ and $\Diamond$, respectively. The corresponding solid symbols show the results from the $\xi = 3$ simulations. The dashed and dotted curves indicate extrapolations to the continuum limit obtained by fitting to the $\xi = 3$ and the $\xi = 5$, respectively (see Tables XVII and XVIII).

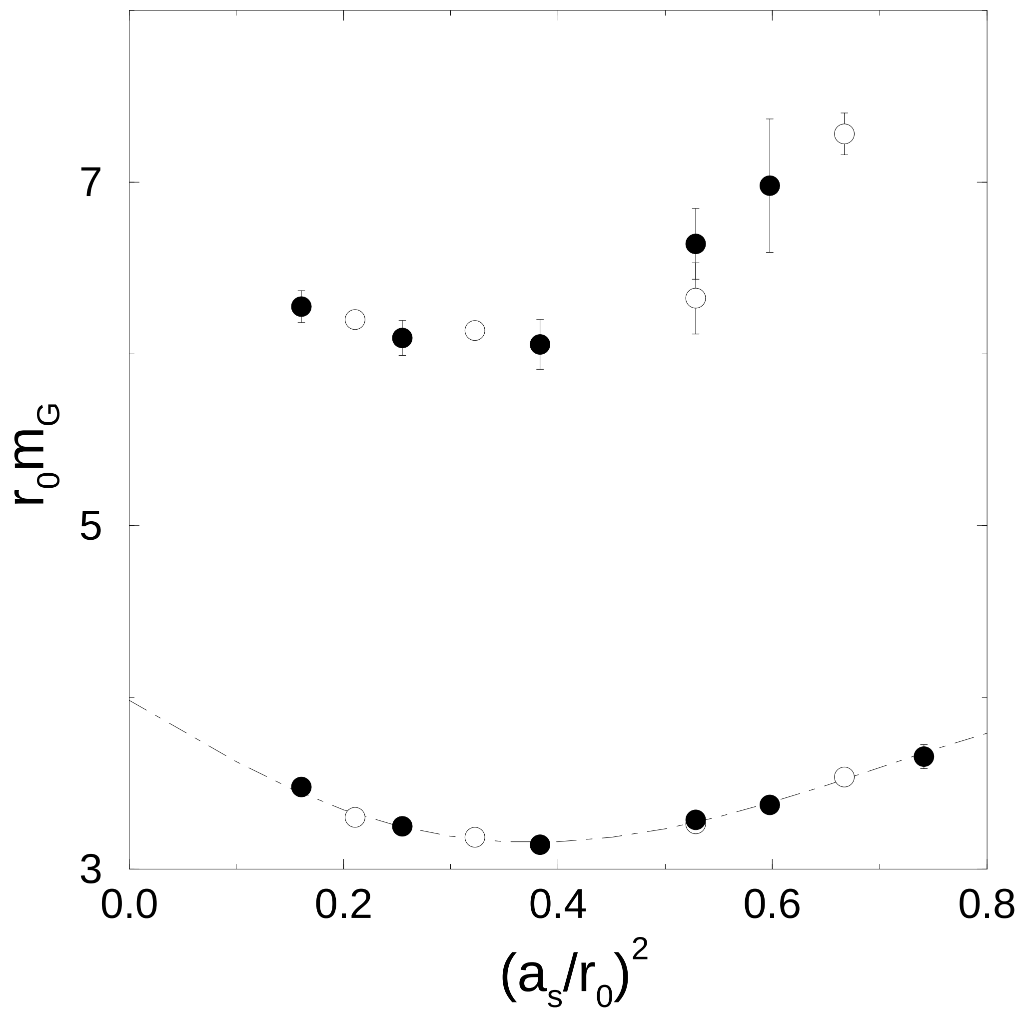

FIG. 14. Masses of the scalar glueball and its first-excited state in terms of r_0 against the lattice spacing $(a_s/r_0)^2$. Open and solid symbols indicate results from the $\xi = 5$ and $\xi = 3$ simulations, respectively. The extrapolation to the continuum limit is indicated by the dash-dotted curve.

TABLES

TABLE I. Input parameters used in the glueball simulations.

β	ξ	Lattice	u_s^4
1.7	3	$6^3 \times 18$	0.3075
1.9	3	$6^3 \times 18$	0.340
2.0	3	$8^3 \times 24$	0.356
2.2	3	$8^3 \times 24$	0.3885
2.4	3	$8^3 \times 24$	0.421
2.6	3	$10^3 \times 30$	0.4505
1.7	5	$6^3 \times 30$	0.295
1.9	5	$6^3 \times 30$	0.328
2.2	5	$8^3 \times 40$	0.378
2.4	5	$8^3 \times 40$	0.409

TABLE II. Various run parameters for the static-quark potential measurements, including lattice sizes, total numbers of configurations used, and parameters for the two different smearing schemes.

β	ξ	Lattice	# configs	$(\lambda_1, n_{\lambda 1})$	$(\lambda_2, n_{\lambda 2})$
1.7	3	$6^3 \times 18$	2275	$(0.05, 4)$	$(0.10, 4)$
1.9	3	$6^3 \times 18$	1280	$(0.07, 4)$	$(0.14, 4)$
2.0	3	$8^3 \times 24$	848	$(0.07, 4)$	$(0.15, 4)$
2.2	3	$8^3 \times 24$	1024	$(0.10, 6)$	$(0.16, 6)$
2.4	3	$8^3 \times 24$	1024	$(0.12, 6)$	$(0.25, 6)$
2.6	3	$10^3 \times 30$	1100	$(0.25, 6)$	$(0.50, 6)$
1.7	5	$8^3 \times 40$	810	$(0.10, 6)$	$(0.25, 6)$
1.9	5	$6^3 \times 30$	1024	$(0.08, 4)$	$(0.16, 4)$
2.2	5	$12^3 \times 48$	315	$(0.20, 4)$	$(0.30, 4)$
2.4	5	$8^3 \times 40$	548	$(0.20, 6)$	$(0.40, 6)$

TABLE III. Results for the hadronic scale r_0 in terms of the lattice spacing a_s. The Coulombic coupling e_c and the string tension σ obtained from a fit of the on-axis potential to a Coulomb plus linear form $V(\vec{r}) = e_c/r + \sigma r + V_0$ are also given.

β	ξ	r_0/a_s	a_s/r_0	e_c	$r_0^2\sigma$
1.7	3	1.161(2)	0.861(2)	$-0.07(1)$	1.58(1)
1.9	3	1.293(3)	0.773(2)	$-0.13(2)$	1.52(2)
2.0	3	1.375(1)	0.7271(8)	$-0.188(7)$	1.462(7)
2.2	3	1.615(2)	0.6192(8)	$-0.288(8)$	1.362(8)
2.4	3	1.978(6)	0.505(1)	$-0.321(6)$	1.329(6)
2.6	3	2.487(5)	0.4021(9)	$-0.310(2)$	1.340(2)
1.7	5	1.224(1)	0.8169(9)	$-0.177(9)$	1.473(9)
1.9	5	1.375(2)	0.727(1)	$-0.20(1)$	1.45(1)
2.2	5	1.761(2)	0.5680(5)	$-0.294(4)$	1.356(4)
2.4	5	2.180(6)	0.459(1)	$-0.308(4)$	1.342(4)

TABLE IV. Results from fits to the $\beta = 1.7$, $\xi = 3$ glueball correlators. N_{exp} is the number of exponentials used in each fit, and the fit range refers to the temporal separations $t_{\rm min} - t_{\rm max}$ used in each fit. Q is the standard quality of fit. Energies are given in a_t^{-1}. Final mass estimates are highlighted in boldface.

Channel	N_{exp}	fit range	χ^2/dof	Q	energies	overlaps
A_1^{++}	1	$0-5$	0.71	0.58	1.061(7)	1.000(4)
	1	$1-5$	0.83	0.48	**1.05(2)**	0.99(2)
	1	$2-5$	1.20	0.30	1.04(5)	0.96(9)
E^{++}	1	$0-3$	0.02	0.98	1.653(8)	1.000(3)
	1	$1-4$	0.12	0.88	**1.65(5)**	1.00(5)
	2	$1-3$	1.37	0.25	1.65(5)	0.98(5)
					2.5(2)	1.1(2)
T_2^{++}	1	$0-3$	0.60	0.55	1.99(1)	1.000(2)
	1	$1-3$	0.06	0.81	**1.92(6)**	0.94(6)
	2	$1-3$	0.65	0.58	1.90(6)	0.88(8)
					2.5(3)	0.8(3)
T_1^{+-}	1	$1-3$	0.62	0.43	**2.09(9)**	0.95(8)

TABLE V. Results from fits to the $\beta = 1.9$, $\xi = 3$ glueball correlators (see Table IV).

Channel	N_{exp}	fit range	χ^2/dof	Q	energies	overlaps
A_1^{++}	1	$0-4$	1.05	0.37	0.878(6)	1.000(5)
	1	$1-4$	1.46	0.23	**0.87(1)**	0.99(1)
	2	$1-3$	0.74	0.53	0.88(1)	1.00(1)
					1.8(1)	1.0(1)
E^{++}	1	$0-4$	0.11	0.95	1.493(9)	1.000(3)
	1	$1-4$	0.04	0.96	**1.47(4)**	0.98(3)
	2	$1-3$	0.06	0.98	1.47(4)	0.95(5)
					1.9(1)	0.91(9)
T_2^{++}	1	$0-3$	1.74	0.18	1.681(8)	1.000(2)
	1	$1-3$	0.22	0.64	**1.60(4)**	0.92(4)
	2	$1-3$	0.23	0.88	1.58(4)	0.88(4)
					2.6(2)	1.3(3)
T_1^{+-}	1	$1-3$	0.24	0.63	**1.80(6)**	0.90(5)

TABLE VI. Results from fits to the $\beta = 2.0$, $\xi = 3$ glueball correlators (see Table IV).

Channel	N_{exp}	fit range	χ^2/dof	Q	energies	overlaps
A_1^{++}	1	$0-6$	0.94	0.45	0.794(4)	1.000(4)
	1	$1-6$	1.15	0.33	**0.797(9)**	1.002(9)
	2	$1-3$	2.33	0.07	0.794(8)	1.001(8)
					1.61(5)	0.95(5)
E^{++}	1	$0-4$	0.67	0.57	1.423(6)	1.000(2)
	1	$1-4$	0.42	0.65	**1.40(2)**	0.97(2)
	2	$1-3$	1.30	0.27	1.39(2)	0.96(2)
					1.81(6)	0.94(5)
T_2^{++}	1	$0-4$	2.54	0.05	1.559(5)	1.000(2)
	1	$1-4$	0.67	0.51	**1.49(2)**	0.94(2)
	2	$1-3$	0.53	0.66	1.49(2)	0.94(2)
					2.11(7)	1.01(7)
T_1^{+-}	1	$1-4$	0.02	0.98	**1.68(3)**	0.92(3)

TABLE VII. Results from fits to the $\beta = 2.2$, $\xi = 3$ glueball correlators (see Table IV).

Channel	N_{exp}	fit range	χ^2/dof	Q	energies	overlaps
A_1^{++}	1	$0-7$	1.12	0.35	0.659(4)	0.998(6)
	1	$1-7$	0.76	0.58	**0.649(8)**	0.988(8)
	2	$1-4$	1.02	0.41	0.647(8)	0.984(8)
					1.25(3)	0.93(2)
E^{++}	1	$1-4$	0.10	0.90	**1.19(2)**	0.95(2)
	1	$2-4$	0.10	0.75	1.17(6)	0.9(1)
	2	$1-3$	0.32	0.81	1.19(2)	0.95(2)
					1.62(4)	0.99(4)
T_2^{++}	1	$0-4$	2.32	0.07	1.280(6)	1.001(2)
	1	$1-4$	0.92	0.40	**1.24(2)**	0.96(2)
	1	$2-4$	0.02	0.88	1.16(6)	0.8(1)
	2	$1-3$	1.30	0.27	1.24(2)	0.96(2)
					1.65(5)	0.87(4)
T_1^{+-}	1	$1-4$	1.13	0.32	**1.48(3)**	0.98(3)

TABLE VIII. Results from fits to the $\beta = 2.4$, $\xi = 3$ glueball correlators (see Table IV).

Channel	N_{exp}	fit range	χ^2/dof	Q	energies	overlaps
A_1^{++}	1	$1-8$	0.19	0.98	**0.548(6)**	0.988(6)
	1	$2-8$	0.22	0.96	0.550(9)	0.99(2)
	2	$1-4$	1.12	0.35	0.550(6)	0.991(6)
					1.03(2)	0.96(1)
E^{++}	1	$0-5$	1.30	0.27	1.012(4)	1.000(3)
	1	$1-5$	0.31	0.82	**0.995(9)**	0.982(9)
	2	$1-3$	2.14	0.09	0.993(8)	0.982(8)
					1.37(2)	1.00(2)
T_2^{++}	1	$0-5$	3.98	0.00	1.035(4)	1.001(2)
	1	$1-5$	0.28	0.84	**1.006(8)**	0.969(9)
	2	$1-3$	0.53	0.66	1.006(8)	0.966(8)
					1.42(2)	0.99(2)
T_1^{+-}	1	$1-4$	0.75	0.47	**1.24(1)**	0.98(1)

TABLE IX. Results from fits to the $\beta = 2.6$, $\xi = 3$ glueball correlators (see Table IV).

Channel	N_{exp}	fit range	χ^2/dof	Q	energies	overlaps
A_1^{++}	1	$1-10$	0.88	0.53	**0.464(7)**	0.986(8)
	1	$2-10$	1.01	0.42	0.46(1)	0.98(2)
	2	$1-4$	0.89	0.50	0.464(6)	0.988(8)
					0.84(1)	0.96(1)
E^{++}	1	$1-6$	0.60	0.67	**0.781(8)**	0.984(8)
	1	$2-6$	0.36	0.78	0.76(2)	0.94(4)
	2	$1-4$	0.89	0.50	0.782(9)	0.982(9)
					1.09(2)	0.95(2)
T_2^{++}	1	$1-6$	0.31	0.87	**0.777(8)**	0.977(8)
	1	$2-6$	0.12	0.95	0.76(2)	0.95(3)
	2	$1-4$	0.53	0.79	0.777(8)	0.976(8)
					1.12(1)	0.99(1)
T_1^{+-}	1	$1-5$	0.27	0.85	**0.97(1)**	0.97(1)

TABLE X. Results from fits to the $\beta = 1.7$, $\xi = 5$ glueball correlators (see Table IV).

Channel	N_{exp}	fit range	χ^2/dof	Q	energies	overlaps
A_1^{++}	1	$0-5$	1.36	0.24	0.585(3)	0.999(4)
	1	$1-5$	0.26	0.86	**0.578(5)**	0.992(5)
	2	$1-4$	0.38	0.89	0.578(5)	0.992(5)
					1.19(2)	0.97(2)
E^{++}	1	$0-5$	2.09	0.08	0.943(3)	1.000(2)
	1	$1-5$	0.12	0.95	**0.924(8)**	0.981(7)
	2	$1-4$	0.29	0.94	0.924(8)	0.979(7)
					1.29(2)	0.98(1)
T_2^{++}	1	$0-5$	1.25	0.29	1.107(3)	1.001(2)
	1	$1-5$	1.58	0.19	**1.103(8)**	0.997(9)
	2	$1-4$	0.87	0.52	1.104(9)	0.997(9)
					1.41(2)	0.94(2)
T_1^{+-}	1	$0-3$	2.65	0.07	1.214(4)	1.000(2)
	1	$1-3$	0.21	0.65	**1.19(1)**	0.97(1)
	2	$1-3$	0.39	0.76	1.18(1)	0.97(1)
					1.55(3)	0.92(2)

TABLE XI. Results from fits to the $\beta = 1.9$, $\xi = 5$ glueball correlators (see Table IV).

Channel	N_{exp}	fit range	χ^2/dof	Q	energies	overlaps
A_1^{++}	1	$1-9$	1.26	0.26	**0.475(4)**	0.992(5)
	1	$2-9$	1.11	0.35	0.468(6)	0.98(1)
	2	$2-4$	1.03	0.38	0.468(6)	0.98(1)
					0.92(3)	0.85(5)
E^{++}	1	$1-6$	0.42	0.80	**0.844(6)**	0.992(6)
	1	$2-6$	0.20	0.90	0.83(1)	0.97(2)
	2	$1-4$	0.69	0.66	0.844(6)	0.992(6)
					1.09(1)	0.95(1)
T_2^{++}	1	$1-5$	0.91	0.43	**0.918(7)**	0.982(6)
	1	$2-5$	1.11	0.33	0.91(2)	0.96(3)
	2	$1-4$	1.44	0.19	0.918(6)	0.981(6)
					1.23(1)	0.96(1)
T_1^{+-}	1	$1-5$	0.30	0.83	**1.053(8)**	0.979(7)
	1	$2-5$	0.18	0.84	1.04(2)	0.95(4)
	2	$1-4$	0.48	0.82	1.052(9)	0.97(1)
					1.30(1)	0.92(1)

TABLE XII. Results from fits to the $\beta = 2.2$, $\xi = 5$ glueball correlators (see Table IV).

Channel	N_{exp}	fit range	χ^2/dof	Q	energies	overlaps
A_1^{++}	1	$1-14$	0.60	0.84	**0.362(3)**	0.998(5)
	1	$2-14$	0.50	0.90	0.366(4)	1.004(7)
	2	$1-4$	0.86	0.52	0.362(3)	0.998(5)
					0.697(6)	0.970(7)
E^{++}	1	$1-7$	1.33	0.25	**0.667(4)**	0.982(4)
	1	$2-7$	1.65	0.16	0.666(7)	0.98(1)
	2	$1-4$	0.57	0.75	0.667(4)	0.980(5)
					0.878(7)	0.968(7)
T_2^{++}	1	$1-8$	1.05	0.39	**0.686(4)**	0.983(3)
	1	$2-8$	1.20	0.31	0.683(6)	0.98(1)
	2	$1-4$	0.77	0.59	0.686(3)	0.982(3)
					0.938(5)	0.970(5)
T_1^{+-}	1	$1-6$	0.48	0.75	**0.819(4)**	0.974(4)
	1	$2-6$	0.57	0.63	0.82(1)	0.98(2)
	2	$1-4$	0.60	0.73	0.820(4)	0.974(4)
					1.025(8)	0.956(7)

TABLE XIII. Results from fits to the $\beta = 2.4$, $\xi = 5$ glueball correlators (see Table IV).

Channel	N_{exp}	fit range	χ^2/dof	Q	energies	overlaps
A_1^{++}	1	$1-13$	1.35	0.19	**0.303(3)**	0.995(7)
	1	$2-13$	1.15	0.32	0.307(4)	1.000(8)
	2	$1-5$	0.86	0.56	0.304(3)	0.994(7)
					0.569(4)	0.972(5)
E^{++}	1	$1-9$	1.33	0.23	**0.538(3)**	0.992(3)
	1	$2-9$	1.46	0.19	0.536(5)	0.986(9)
	2	$2-5$	2.71	0.01	0.538(5)	0.99(1)
					0.723(9)	0.94(1)
T_2^{++}	1	$1-9$	1.08	0.38	**0.542(2)**	0.988(3)
	1	$2-7$	0.34	0.85	0.540(4)	0.982(7)
	2	$2-5$	1.28	0.26	0.538(4)	0.978(8)
					0.730(8)	0.94(1)
T_1^{+-}	1	$2-6$	1.03	0.38	**0.652(5)**	0.95(1)
	2	$2-6$	1.77	0.07	0.648(6)	0.95(1)
					0.794(9)	0.88(2)

TABLE XIV. Summary of final mass estimates from all $\xi = 3$ and $\xi = 5$ simulations.

β	ξ	$a_t m(A_1^{++})$	$a_t m(E^{++})$	$a_t m(T_2^{++})$	$a_t m(T_1^{+-})$
1.7	3	1.05(2)	1.65(5)	1.92(6)	2.09(9)
1.9	3	0.87(1)	1.47(4)	1.60(4)	1.80(6)
2.0	3	0.797(9)	1.40(2)	1.49(2)	1.68(3)
2.2	3	0.649(8)	1.19(2)	1.24(2)	1.48(3)
2.4	3	0.548(6)	0.995(9)	1.006(8)	1.24(1)
2.6	3	0.464(7)	0.781(8)	0.777(8)	0.97(1)
1.7	5	0.578(5)	0.924(8)	1.103(8)	1.19(1)
1.9	5	0.475(4)	0.844(6)	0.918(7)	1.053(8)
2.2	5	0.362(3)	0.667(4)	0.686(4)	0.819(4)
2.4	5	0.303(3)	0.538(3)	0.542(2)	0.652(5)

TABLE XV. Glueball mass estimates in terms of a_t^{-1} for $\beta = 2.4$, $\xi = 3$ and various lattice volumes.

Channel	$L_s/a_s = 4$	$L_s/a_s = 5$	$L_s/a_s = 6$	$L_s/a_s = 8$
A_1^{++}	0.483(6)	0.551(6)	0.545(8)	0.548(6)
A_1^{*++}	0.863(9)	0.97(1)	1.00(3)	1.027(17)
E^{++}	0.848(9)	0.980(10)	1.004(19)	0.995(9)
E^{*++}	1.11(2)	1.27(2)	1.41(4)	1.37(2)
$T2^{++}$	1.032(9)	1.005(9)	1.002(14)	1.006(8)
$T2^{*++}$	1.37(2)	1.42(2)	1.40(3)	1.42(2)
$T1^{+-}$	1.245(13)	1.235(11)	1.209(25)	1.237(14)

TABLE XVI. The effects of simulating in a finite box: results from fits of Eq. 16 to the energy estimates given in Table XV from lattices of spatial extent $L_s/a_s = 4, 5, 6, 8$. The T_1^{+-} fit also includes an energy estimate for $L_s/a_s = 3$. The final column estimates the expected finite-volume errors in glueball masses from the $L_s/a_s = 8$ simulation at $\beta = 2.4$ and $\xi = 3$. These errors are estimated by $m_G(8\omega\xi)/m_G(\infty) - 1$ using Eq. 16.

Channel	$a_t m_G(\infty)$	λ_G	χ^2/dof	% correction
A_1^{++}	0.554(4)	260(37)	2.3	-0.020
E^{++}	1.002(7)	319(23)	0.62	-0.024
T_2^{++}	1.003(6)	$-59(24)$	0.15	$+0.004$
T_1^{+-}	1.223(7)	$-66(4)$	1.05	$+0.005$

TABLE XVII. Extrapolations of the glueball mass estimates to the continuum limit for the $\xi = 3$ runs. The three scaling forms φ_0, φ_2, and φ_4 which are fit to the data are given in Eqs. 17, 18 and 19. The values indicated in bold are taken as our final continuum mass estimates.

Channel	fit function	$r_0 m_G$	c_2	c_4	χ^2/dof
E^{++}	φ_0	5.83(3)	—	—	0.71
	φ_2	5.91(7)	−0.26(20)	—	0.49
	φ_4	**5.87(5)**	—	−0.33(25)	0.46
T_2^{++}	φ_0	5.98(3)	—	—	5.35
	φ_2	5.66(7)	1.02(21)	—	0.90
	φ_4	**5.83(5)**	—	1.29(27)	0.87
T_1^{+-}	φ_0	**7.22(5)**	—	—	1.81
	φ_2	7.44(11)	−0.71(31)	—	0.96
	φ_4	7.32(7)	—	−0.87(40)	1.07
E^{*++}	φ_0	7.99(8)	—	—	2.44
	φ_2	8.52(20)	−1.8(6)	—	0.31
	φ_4	**8.25(12)**	—	−2.6(9)	0.12
T_2^{*++}	φ_0	8.37(6)	—	—	1.33
	φ_2	8.32(16)	0.2(7)	—	1.94
	φ_4	**8.34(8)**	—	0.5(11)	1.89

TABLE XVIII. Extrapolations of the glueball mass estimates to the continuum limit for the $\xi = 5$ runs. The three scaling forms φ_0, φ_2, and φ_4 which are fit to the data are given in Eqs. 17, 18 and 19. The values indicated in bold are taken as our final continuum mass estimates.

Channel	fit function	$r_0 m_G$	c_2	c_4	χ^2/dof
E^{++}	φ_0	5.82(2)	—	—	5.03
	φ_2	5.98(5)	−0.41(12)	—	1.55
	φ_4	**5.91(3)**	—	−0.50(14)	0.81
T_2^{++}	φ_0	6.12(2)	—	—	82
	φ_2	5.53(4)	1.69(11)	—	5.16
	φ_4	**5.82(3)**	—	2.02(13)	1.32
T_1^{+-}	φ_0	**7.21(2)**	—	—	1.61
	φ_2	7.09(7)	0.31(16)	—	0.57
	φ_4	7.15(4)	—	0.32(18)	0.80
E^{*++}	φ_0	7.67(4)	—	—	5.88
	φ_2	8.12(14)	−1.2(4)	—	0.02
	φ_4	**7.91(8)**	—	−1.5(4)	0.27
T_2^{*++}	φ_0	8.29(3)	—	—	9.17
	φ_2	7.80(10)	1.3(3)	—	1.37
	φ_4	**8.06(6)**	—	1.4(3)	2.48

TABLE XIX. Extrapolations of the scalar glueball mass estimates to the continuum limit. The fit functions used are given in Eqs. 20 and 21. The value indicated in bold is our final continuum mass estimate for the scalar glueball.

State	fit function	$r_0 m_G$	c_2	c_4	c_L	χ^2/dof
A_1^{++}	φ_{1L}	**3.98(15)**	−18(4)	18(5)	0.96(13)	0.25
	$\varphi_{2,4}$	3.86(8)	−3.5(4)	4.5(5)	—	0.55
A_1^{*++}	$\varphi_{2,4}$	6.93(19)	−5.3(1.1)	8.8(1.4)	—	0.41

TABLE XX. Estimates of r_0^{-1} using results from various quenched lattice simulations with the Wilson gluonic action. The simple average $r_0^{-1} = 410(20)$ MeV of the last column is taken as our estimate.

Source	β	Quark Action	Scale Setting Quantity	a^{-1} (GeV)	r_0^{-1} (MeV)
NRQCD[24]	6.0	NRQCD	$\Upsilon(2S-1S, 1P-1S)$	2.4(1)	434(23)
NRQCD[25]	5.7	NRQCD	$J/\psi(1P-1S)$	1.23(4)	430(16)
LANL[26]	6.0	Wilson	M_ρ	2.330(41)	422(16)
GF11[27]	6.17	Wilson	M_ϕ	2.93(11)	419(17)
JLQCD[28]	6.1	Wilson	$J/\psi(1P-1S)$	2.54(7)	394(13)
JLQCD[28]	6.3	Wilson	$J/\psi(1P-1S)$	3.36(11)	401(14)
JLQCD[29]	6.3	Wilson	M_ρ	3.41(20)	406(24)
FNAL[30]	6.1	FNAL	$J/\psi(1P-1S)$	2.55(8)	395(14)
BLS[31]	6.3	heavy-light	f_π	3.21(9)	383(11)
BLS[31]	6.3	heavy-light	M_ρ	3.44(9)	410(11)
UKQCD[32]	6.2	Wilson	M_ρ	2.77(16)	376(22)